



TECHNISCHE  
UNIVERSITÄT  
MÜNCHEN



WALTHER-  
MEISSNER-  
INSTITUT



BAYERISCHE  
AKADEMIE DER  
WISSENSCHAFTEN

# Fabrication of Low-Loss Josephson Junctions for Quantum Devices

Bachelor's Thesis

Patrick Missale

Supervisor: PD Dr. Frank Deppe

Garching, June 24, 2021

Fakultät für Physik

TECHNISCHE UNIVERSITÄT MÜNCHEN

# Contents

<b>1</b>	<b>Introduction</b>	<b>1</b>
<b>2</b>	<b>Theory</b>	<b>3</b>
2.1	Josephson Junctions . . . . .	3
2.1.1	The Josephson Equations . . . . .	3
2.1.2	Ambegaokar-Baratoff Relation . . . . .	5
2.2	Superconducting Quantum Interference Devices (SQUIDs) . . . . .	6
<b>3</b>	<b>Experimental Techniques</b>	<b>8</b>
3.1	Current Fabrication Process at WMI . . . . .	8
3.1.1	Cleaning Steps . . . . .	8
3.1.2	Spin Coating . . . . .	9
3.1.3	E-beam Lithography . . . . .	10
3.1.4	Development . . . . .	13
3.1.5	Evaporation and Oxidation . . . . .	14
3.1.6	Lift-off Process . . . . .	15
3.2	Measurement of the SQUIDs and Josephson Junctions . . . . .	16
3.3	The Descum Step . . . . .	19
<b>4</b>	<b>Experimental Results</b>	<b>21</b>
4.1	Optimization of the E-Beam Charge Dose . . . . .	21
4.1.1	Optimization of the Double-Layer Resist System PMMA/MA33 and PMMA 950K A2 . . . . .	21
4.1.2	Optimization of the Double-Layer Resist System PMMA/MA33 and 950 PMMA A4 . . . . .	24
4.1.3	Optimized Single Junction Pattern . . . . .	27
4.2	Implementation of the Descum Step . . . . .	29
4.2.1	Realization of a Stable Plasma Beam at PLASSYS . . . . .	29
4.2.2	Testing the Descum Potential of the IBG . . . . .	31
4.2.3	Measurement of the Descumming Effect . . . . .	34
<b>5</b>	<b>Summary and Outlook</b>	<b>38</b>

*Contents*

---

<b>A</b>	<b>Plots</b>	<b>40</b>
A.1	Resistance Measurements of Sample 'JJ12-062-PM' . . . . .	41
A.2	Resistance Measurements of Sample 'JJ12-069-PM' . . . . .	42
A.3	Resistance Measurements of Sample 'JJ12-070-PM' . . . . .	43
A.4	Resistance Measurements of Sample 'JJ12-074-PM' . . . . .	44
<b>B</b>	<b>Final Sample Fabrication Parameters</b>	<b>45</b>
B.1	Substrate cleaning . . . . .	45
B.2	Reactive Ion Etching (R.I.E.) and post R.I.E. cleaning . . . . .	46
B.3	Spin Coating . . . . .	47
B.4	E-beam lithography . . . . .	47
B.5	Development . . . . .	49
B.6	Descumming . . . . .	49
B.7	Evaporation and Oxidation . . . . .	50
B.8	Liftoff . . . . .	51

# List of Figures

2.1	Schematic image of a SIS contact. $S_1$ and $S_2$ are two superconductors separated by an insulating barrier $I$ . The thickness of the insulating barrier between the superconductors is given by ' $d$ '. . . . .	4
2.2	Example for the variation of the Cooper pair density $n_s$ and the gauge-invariant phase gradient $\gamma$ across a one-dimensional Josephson junction extending in x-direction. . . . .	4
2.3	SQUID consisting of a superconducting loop which is interrupted by two Josephson junctions. . . . .	6
3.1	First cleaning steps to remove the protective resist from the silicon substrate [12]. . . . .	9
3.2	R.I.E. treatment of the sample to remove potential resist leftovers [12]. . . . .	9
3.3	Schematic illustration of the double-layer resist system [12]. . . . .	10
3.4	Optical micrograph of a corner of sample 'JJ12-066-PM'. The resist area, which is affected by the e-beam lithography decreases around the corner of the sample, since the corner is less affected by electron scattering from written resist in immediate vicinity happens. . . . .	11
3.5	In the left image, the pattern for a single SQUID can be seen. The big, square shaped structures are the ground planes which are used as contact pads for the resistance measurements. The framed section in the center is the actual SQUID loop and can be seen zoomed in in the right image. . . . .	12
3.6	Crosstype junction pattern. We can clearly see the defined junction area (in cyan) and the undercut (green dashed). . . . .	13
3.7	Left: Schematic illustration of the e-beam lithography in the cross section of the junction area. The yellow area indicates resist with broken polymer chains. The green areas symbolize intact top resist layers, the red areas intact bottom resist layers. The shorter arrows in the center indicate a small charge dose and we can see the undercut with the intact top resist. Right: Location of the cross section in the right image. . . . .	13

*List of Figures*

---

3.8	Schematic illustration of the development process. The yellow area indicates resist with broken polymer chains. The green areas symbolize intact top resist layers, the red areas intact bottom resist layers. The developer is removing most of the resist with the broken polymer chains (central picture), the IPA mainly forms the undercut (right picture). . . . .	14
3.9	Optical micrographs of sample 'SQUID12-057-PM' after the e-beam lithography (left) and the development (right). We can see the silicon substrate on the right image, which shows, that the resist layer got removed on the written structures. . . . .	15
3.10	The evaporation system at WMI. In the left picture, the big cylinder in the back is the evaporation main chamber, the smaller chamber is the load lock for sample transfer. In the right picture, the tilted sample holder during an evaporation process can be seen inside the main chamber. . . . .	16
3.11	Schematic illustration of the evaporation process. The cross section of the scheme is the same as in Fig. 3.7. The evaporated aluminum layers are depicted in light blue, the $\text{AlO}_x$ barrier are depicted in orange.	17
3.12	Schematic illustration of the liftoff process. The red box highlights the actual Josephson junction. The aluminum layers are depicted in light blue, the $\text{AlO}_x$ barrier are depicted in orange. . . . .	17
3.13	Images of a crosstype junction. Left: Optical micrograph of a intact junction. Right: SEM-Image of a junction fabricated and recorded by Christoph Scheuer [12]. . . . .	18
3.14	The wafer probing station at WMI. On the left picture can be seen: A source meter to record the U-I-characteristics, a light source for the microscope and the computer for recordings of the measurements. The actual probing station with the measurement contacts above the sample holder can be seen in the dashed box. A zoomed in image of it can be seen in the right, with a SQUID currently being measured.	19
3.15	Recorded U-I-characteristic of one SQUID of SQUID12-057-PM. The ohmic behaviour can be clearly seen. . . . .	19
3.16	The PLASSYS system at WMI. The ion beam gun for the descumming is located inside the load lock. . . . .	20
4.1	Early SQUID pattern in layout editor. The different colours of each column of the SQUID-triplets indicate different charge doses for the ground planes, the blue numbered boxes indicate different charge doses for the Josephson junctions . . . . .	22

*List of Figures*

---

4.2	Optical micrographs of two SQUID-triplets of sample 'SQUID12-046-PM'. The ground planes in the left picture are written with a charge dose of $6.0 \text{ C/m}^2$ , the structures in the right picture with a charge dose of $6.9 \text{ C/m}^2$ . The decrease of resist leftovers with the increase of the charge dose can clearly be seen. . . . .	23
4.3	Optical micrographs of two SQUID-triplets of sample 'SQUID12-047-PM'. The ground planes on the left picture are written with a charge dose of $6.0 \text{ C/m}^2$ , the structures in the right picture with a charge dose of $6.9 \text{ C/m}^2$ . The decrease of the resist leftovers through the stirring of the rotation of the developer can be clearly seen. . . . .	23
4.4	Optical micrographs of two SQUIDS of sample 'SQUID12-056-PM'. The ground planes on the left picture are written with a charge dose of $9.0 \text{ C/m}^2$ , the structures in the right picture with a charge dose of $10.8 \text{ C/m}^2$ . Even with the higher charge dose, resist leftovers are visible and the junction is not developed. . . . .	24
4.5	Zoomed in micrographs of the junction area of two SQUIDS of sample 'SQUID12-057-PM'. The ground planes on the left picture are written with a charge dose of $11.2 \text{ C/m}^2$ , the structures in the right image with a charge dose of $13.0 \text{ C/m}^2$ . In the right image, the edges are well developed and barely any resist leftovers can be seen. In both images the junctions look well developed. . . . .	25
4.6	E-beam patterns with (right) and without (left) proximity effect correction (PEC) by BEAMER. The blue and brown surroundings from the uncorrected pattern are merged with the big ground plane layer to the reference layer. The structures around the junctions are fractured into different layers by BEAMER and get assigned different charge doses. . . . .	26
4.7	SQUIDS of sample 'SQUID12-057-PM' after liftoff. On the left image we can observe an overview of the SQUID-triplet. On the right image, a zoom into the red framed junction area of the left SQUID can be seen. The two offset aluminum layers of the shadow evaporation can also be seen. . . . .	26
4.8	SQUID-resistances of sample 'SQUID12-057-PM'. Three columns together equal one SQUID-triplet. Each SQUID-triplet is written with a different charge dose. Every third column is coloured nearly completely white, since the used SQUID-design is designed for lower charge doses and therefore results in a short-circuited aluminium structure. Column 9 has the most uniform junction resistance and is framed red. . . . .	27
4.9	Short circuited ground planes. The structure equals the normal junction structures, only the Josephson junction itself is removed and a direct aluminium bridge is inserted. . . . .	28

*List of Figures*

---

4.10	Section of the optimized single junction pattern. On the left one junction triplet can be seen, with PEC in the left and middle junction and one uncorrected comparative junction on the left. In the right image a zoom of the junction area itself can be seen, as well as the fractured pattern due to the PEC. Only the junction and a square-shaped area of the ground plane receive PEC. . . . .	28
4.11	Josephson junctions of sample 'JJ12-064-PM' after development (left) and after liftoff (right). The junction is well defined, only on the ground plane on the top resist residues can be seen, the PEC area of the ground plane seems to use a too small charge dose. . . . .	29
4.12	AFM image of sample 'JJ12-063-PM' before the application of the first descumming. The dark regions symbolize lower located regions and therefore developed areas, the brighter parts symbolize higher located regions and therefore the not written remaining resist. The red line in the center indicates the area used for the measurement of the resist height. . . . .	32
4.13	AFM images and evaluation of the PEC area of the ground plane of sample 'JJ12-063-PM'. In the upper pictures, the resist leftovers are highlighted as a mask in blue for the sample before (left) and after (right) the descumming using an auto-thresholding function. In the lower pictures the counted resist leftovers of the mask before (left) and after (right) the descumming are plotted against the measured height. . . . .	33
4.14	Relative resistance change for the PEC-junctions of sample 'JJ12-062-PM'. The tendency of a resistance decrease is clearly visible. More detailed plots can be found in Appendix A.1 . . . . .	34
4.15	Relative resistance changes of samples 'JJ12-069-PM' (blue), 'JJ12-070-PM' (green) and 'JJ12-074-PM' (red). More detailed plots of the individual samples can be found in the Appendix in Figs. A.2,A.3 and A.4 . . . . .	36
A.1	Absolute resistance values measured before and after annealing sample 'JJ12-062-PM'. The two left figures are the measurements before annealing, the two right figures are the measurements after annealing. In the bar chart, only the PEC junctions are listed, the short circuited junctions (three dark rows of the colorplot) and the non PEC junctions are not further investigated. . . . .	41
A.2	Resistance change due to the annealing of sample 'JJ12-062-PM'. In the bar chart, only the PEC junctions are listed, the short circuited junctions (seen in the three dark rows of the colorplot) and the non PEC junctions are not further investigated. . . . .	41

*List of Figures*

---

A.3	Absolute resistance values measured before and after annealing sample 'JJ12-069-PM'. The two left figures are the measurements before annealing, the two right figures are the measurements after annealing. . . . .	42
A.4	Calculated resistance change due to the annealing of sample 'JJ12-069-PM'. . . . .	42
A.5	Absolute resistance values measured before and after annealing sample 'JJ12-070-PM'. The two left figures are the measurements before annealing, the two right figures are the measurements after annealing. . . . .	43
A.6	Calculated resistance change due to the annealing of sample 'JJ12-070-PM'. . . . .	43
A.7	Absolute resistance values measured before and after annealing sample 'JJ12-074-PM'. The two left figures are the measurements before annealing, the two right figures are the measurements after annealing. . . . .	44
A.8	Calculated resistance change due to the annealing of sample 'JJ12-074-PM'. . . . .	44
B.1	Relative charge doses for each layer of the e-beam pattern file 'JJ12-062-PM.gds'. Each relative charge dose has to be multiplied with a reference charge dose to receive the absolute charge dose. . . . .	48

# List of Tables

4.1	Values for different parameters of the plasma beam used for descumming with the IBG at PLASSYS. The left column shows the values used at KIT [18], the columns labelled with 'test' are mentioned in Sec. 4.2.2. . . . .	31
4.2	Used descum parameters for the different samples. Only the samples 'JJ12-069-PM', 'JJ12-070-PM' and 'JJ12-074-PM' are used for evaporation, resistance measurement, annealing and a second resistance measurement after the annealing. . . . .	35
B.1	Cleaning steps for the silicon substrates. The sample is put into the supersonic inside a beaker with isopropanol and afterwards blown dry with a N <sub>2</sub> gun. . . . .	45
B.2	R.I.E. parameters for the ashing of the silicon substrates. . . . .	46
B.3	Cleaning steps for the silicon substrates after the R.I.E. treatment . . . . .	46
B.4	Spin coating parameters for the top and bottom resist. . . . .	47
B.5	Parameters for the e-beam lithography. The reference charge dose has to be multiplied with the relative charge dose of each layer to receive the absolute charge dose. The relative charge doses can be found in Fig. B.1 . . . . .	47
B.6	Parameters for the development of the sample. The sample is held into the beaker with AR 600-56 facing down with the side with the written structures. The IPA is kept between 4° and 4.5° with a peltier cooler. . . . .	49
B.7	Descumming parameters used for the ion beam gun (IBG) in PLASSYS. The bold parameters were set as input, the other parameters could not be varied and only the measured parameter values are listed. . . . .	49
B.8	Evaporation and oxidation parameters at the Alu-EVAP. . . . .	50
B.9	Parameters for the liftoff of the evaporated samples. . . . .	51

# Chapter 1

## Introduction

For many years, quantum sciences and the underlying quantum physics have been seen as a complex field of research with hardly any relation to the real application. This view has changed over the years. Especially during the last decades, quantum technologies are no longer of pure scientific, but also increasingly of industrial interest [1]. More and more governments of the industrial countries support research of quantum technologies in their own country, i.e. the EU funded their 'quantum flagship' with up to 1 billion Euro in 2018 [2][3], the USA signed the 'National Quantum Initiative act' in 2018 [4][5] and China increased its funds into quantum technologies from 10 million dollar from 1998 to 2006 up to 490 million dollar from 2011 to 2015 [6].

Quantum technologies include many different fields of research and applications. Research in Germany focuses on the three major fields quantum computing, quantum communication and quantum based measurement technology [7]. One of the most promising platforms for realizing these various quantum technologies are superconducting quantum circuits. In these, qubits serve as artificial atoms with two-level-system properties [8]. While there are many examples of naturally occurring two-level systems, e.g., ion traps, Josephson-junction-based superconducting circuits have turned out to be especially advantageous in terms of scalability and design flexibility [9]. In particular with respect to scalability, the reproducibility of Josephson junctions with suitable parameters relies heavily on their fabrication process and they determine the properties of the resulting qubit in terms of its coherence time, qubit frequency and more.

In this thesis, different steps of the fabrication process of Josephson junctions at the Walther-Meissner-Institut (WMI) are investigated and optimized. Additionally, the fabrication process is expanded by a descum step, which removes impurities on the Josephson junctions and therefore increases the quality and the properties of the junctions.

This thesis is structured in the following way: First, a short summarization of the theoretical background of superconductivity, Josephson junctions and SQUIDs is given in chapter 2, followed by a presentation of the so far established and optim-

ized fabrication process of Josephson junctions at WMI in chapter 3. In chapter 4, adaptations and improvements of the fabrication process are presented, which become necessary due to the use of larger  $12\text{ mm} \times 12\text{ mm}$  silicon substrates, compared to the so far used  $10\text{ mm} \times 6\text{ mm}$  substrates. The chapter ends with the first steps of implementing a new fabrication step, the descumming. In chapter 5, the improvements and insights gained during the course of this thesis are summarized and an outlook for further improvements of the fabrication process is given.

# Chapter 2

## Theory

### 2.1 Josephson Junctions

The integral part of modern qubits are Josephson junctions, based on the Josephson effect predicted by Brian Josephson in 1962, which describes the coherent tunneling of Cooper pairs through a tunnel barrier. In the following sections, the behaviour of a superconductor-insulator-superconductor (SIS) contact in different settings is discussed and the basic Josephson equations and behaviours are presented. Some steps of the derivations are skipped and can be viewed in [10].

#### 2.1.1 The Josephson Equations

An illustration of a SIS contact can be seen in Fig. 2.1. Each superconductor can be described by a macroscopic wave function  $\Psi_i = \sqrt{n_{s,i}}e^{i\theta_i}$ . The absolute value of the squared amplitude  $|\Psi_i|^2$  equals the density of the Cooper pairs  $n_{s,i}$  inside the superconductors and  $\theta_i$  the global phase of the wave function for each superconductor.

Due to the overlap of the wavefunctions across the insulating barrier with thickness  $d$ , the density of Cooper pairs inside the insulator takes on a finite value, which results in a measurable Josephson current  $J_s$  across the SIS contact. The dependence of the supercurrent on the phases  $\theta_1$  and  $\theta_2$  can be seen in the equation for the supercurrent density in a bulk superconductor:

$$J_s(\mathbf{r}, t) = \frac{q_s n_s \hbar}{m_s} \cdot \left( \nabla \theta(\mathbf{r}, t) - \frac{2\pi}{\Phi_0} \mathbf{A}(\mathbf{r}, t) \right) = \frac{q_s n_s \hbar}{m_s} \cdot \gamma(\mathbf{r}, t). \quad (2.1)$$

Here,  $\Phi_0$  is the magnetic flux quantum,  $q_s = 2e$  is the charge and  $m_s = 2m_e$  the mass of a Cooper pair. Due to current preservation,  $J_s$  has the same value inside of the superconductors and the insulating barrier while the density of cooper pairs decreases  $n_s$  outside of the superconductors, therefore the gauge-invariant phase gradient  $\gamma$

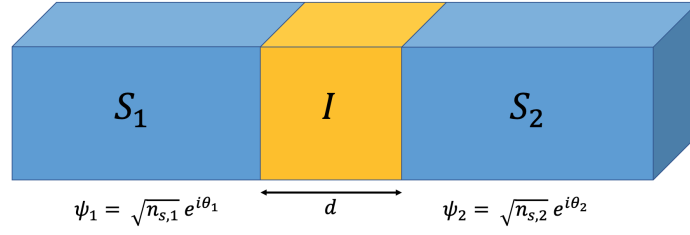


**Figure 2.1:** Schematic image of a SIS contact.  $S_1$  and  $S_2$  are two superconductors separated by an insulating barrier  $I$ . The thickness of the insulating barrier between the superconductors is given by ' $d$ '.

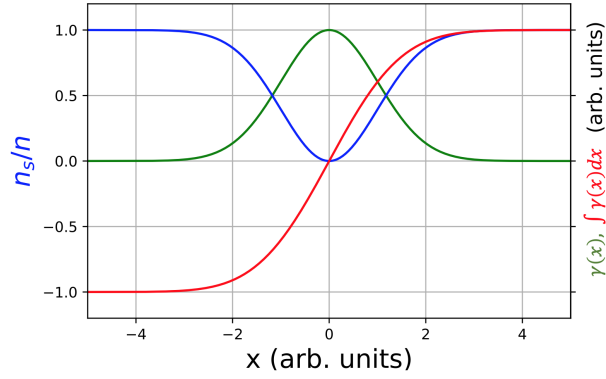


**Figure 2.2:** Example for the variation of the Cooper pair density  $n_s$  and the gauge-invariant phase gradient  $\gamma$  across a one-dimensional Josephson junction extending in  $x$ -direction.

increases inside of the barrier, as shown in Fig. 2.2. Since  $\gamma$  is sufficiently small in the superconductors the phase gradient  $\gamma$  can be replaced by the gauge-invariant phase  $\varphi$ , given by

$$\varphi = \int_1^2 \gamma(\mathbf{r}, t) d\mathbf{l} = \int_1^2 \left( \nabla\theta(\mathbf{r}, t) - \frac{2\pi}{\Phi_0} \mathbf{A}(\mathbf{r}, t) \right) d\mathbf{l} = \theta_2(\mathbf{r}, t) - \theta_1(\mathbf{r}, t) - \frac{2\pi}{\Phi_0} \int_1^2 \mathbf{A}(\mathbf{r}, t) d\mathbf{l}. \quad (2.2)$$

The integration path is along the direction of the supercurrent ( $x$ -direction in Fig. 2.1). The gauge-invariant phase  $\varphi$  is symbolized by the height difference of the plateaus of the red curve in Fig. 2.2.

Theoretical considerations and measurements lead to the first Josephson equation, also known as the current-phase relation, which defines the relation between the

supercurrent density  $J_c$  and the gauge-invariant phase  $\varphi$ .

$$J_s = J_c \sin \varphi, \quad (2.3)$$

where  $J_c$  is the critical or maximum Josephson current density. It can be seen that the supercurrent density across a Josephson junction varies sinusoidally with the phase difference  $\varphi$ , which in the absence of any scalar and vector potentials is given by  $\varphi = \theta_2 - \theta_1$ .

In order to obtain the second Josephson equation, the time derivative of the gauge-invariant phase  $\varphi$  from Eq. (2.2)

$$\frac{\partial \varphi}{\partial t} = \frac{\partial \theta_2(\mathbf{r}, t)}{\partial t} - \frac{\partial \theta_1(\mathbf{r}, t)}{\partial t} - \frac{2\pi}{\Phi_0} \frac{\partial}{\partial t} \int_1^2 \mathbf{A}(\mathbf{r}, t) \cdot d\mathbf{l} \quad (2.4)$$

is combined with the energy-phase relation for superconductors

$$-\hbar \frac{\partial \theta}{\partial t} = \frac{1}{2n_s} \Lambda \mathbf{J}_s^2 + q_s \Phi. \quad (2.5)$$

Substitution of Eq. (2.5) into Eq. (2.4) and considering that  $\mathbf{J}_s^2(1)$  equals  $\mathbf{J}_s^2(2)$  due to current preservation across the junction, we obtain the second Josephson equation, also known as the voltage-phase relation:

$$\frac{\partial \varphi}{\partial t} = \frac{2\pi}{\Phi_0} \int_1^2 \mathbf{E}(\mathbf{r}, t) \cdot d\mathbf{l} = \frac{2\pi}{\Phi_0} U. \quad (2.6)$$

Here,  $U$  corresponds to the voltage drop across the junction. An externally applied voltage drives the time evolution of the phase difference  $\varphi$ .

### 2.1.2 Ambegaokar-Baratoff Relation

A useful equation for the measurement of the critical Josephson current density  $J_c$  is the 1963 by Vinay Ambegaokar and Alexis Baratoff derived 'Ambegaokar-Baratoff-relation'. It connects the critical Josephson current across one Josephson junction with the measured resistance at room temperature, which therefore allows the derivation of the critical Josephson current density without the need of a cryogenic measurement setup. The relation can be seen below

$$R_n \cdot I_c = \frac{\pi}{2e} \cdot \Delta(T) \cdot \tanh \frac{\Delta(T)}{2k_B \cdot T}, \quad (2.7)$$

with  $\Delta(T)$  the superconducting energy gap at temperature  $T$ ,  $k_B$  the Boltzmann constant and  $I_c$  the total critical current across the junction and  $I_c = J_c \cdot A$ , where  $A$  is the junction area [11].

## 2.2 Superconducting Quantum Interference Devices (SQUIDs)

A common application for Josephson junctions is the construction of SQUIDs out of one or more single junctions. SQUIDs are highly sensitive magnetic flux detectors and find many applications in superconducting quantum circuits.

In Fig. 2.3 a schematic image of a SQUID can be seen.

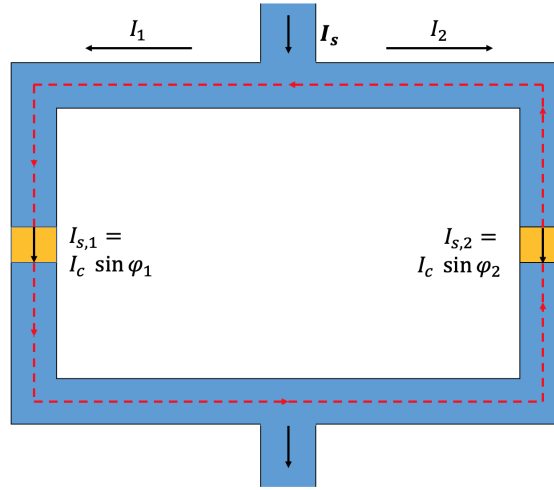


**Figure 2.3:** SQUID consisting of a superconducting loop which is interrupted by two Josephson junctions.

To simplify the system, we assume two identical Josephson junctions with identical critical current  $I_c$ . Their current-phase relations are given by  $I_{s,1} = I_c \cdot \sin(\varphi_1)$  and  $I_{s,2} = I_c \cdot \sin(\varphi_2)$ , the total current transmitted across the junction is given by

$$\begin{aligned} I_s &= I_{s,1} + I_{s,2} = I_c \cdot \sin(\varphi_1) + I_c \cdot \sin(\varphi_2) \\ &= 2I_c \cdot \cos\left(\frac{\varphi_1 - \varphi_2}{2}\right) \sin\left(\frac{\varphi_1 + \varphi_2}{2}\right). \end{aligned} \quad (2.8)$$

Here, the gauge-invariant phase differences  $\varphi_i$  are not independent from each other,

since the phase change along the closed red path seen in Fig. 2.3 has to be  $2\pi n$ :

$$\oint_C \nabla\theta = 2\pi n. \quad (2.9)$$

# Chapter 3

## Experimental Techniques

### 3.1 Current Fabrication Process at WMI

The fabrication process of Josephson junctions, SQUIDs and resonators at WMI consists of multiple steps, whose parameters have to be optimized separately. Since other students already investigated a reproducible fabrication process [12][13][14][15][16], many parameters could be adopted. To gain more statistics in the measurements, larger silicon substrates than before were used. The change from  $10\text{ mm} \times 6\text{ mm}$  to  $12\text{ mm} \times 12\text{ mm}$  makes the optimization of some steps during this thesis necessary.

#### 3.1.1 Cleaning Steps

The used silicon substrates have a thickness of  $525\text{ }\mu\text{m}$ , a specific resistivity greater than  $4000\text{ }\Omega\text{cm}$  and the crystal orientation is [100]. They are coated with a protective resist to prevent damages on the silicon surface. In the first cleaning steps, this protective resist needs to be removed.

Therefore the substrate is put into acetone at  $70^\circ\text{C}$  for 10 minutes twice and after that into isopropanol (IPA) at room temperature. The sample in the IPA is placed in a strong supersonic bath for two minutes. A schematic illustration of the first cleaning steps can be found in Fig. 3.1.

Afterwards, to remove remaining resist leftovers the silicon substrates are handled by a R.I.E. (Reactive Ion Etching) treatment. In an evacuated chamber, oxygen plasma is deployed on the substrate with a flow of  $50\text{ sccm}$ . Those oxygen radicals combine with resist leftovers and form ashes [12], that get removed by the vacuum pumps. That is also, why this process is called 'plasma ashing'. After the R.I.E. treatment, the substrate is put into acetone at  $70^\circ\text{C}$  for 10 minutes and is put into IPA at room temperature. The sample in the IPA is placed in a strong supersonic bath for 2 minutes, which concludes the cleaning process. A schematic illustration of the R.I.E. treatment can be found in Fig. 3.2.

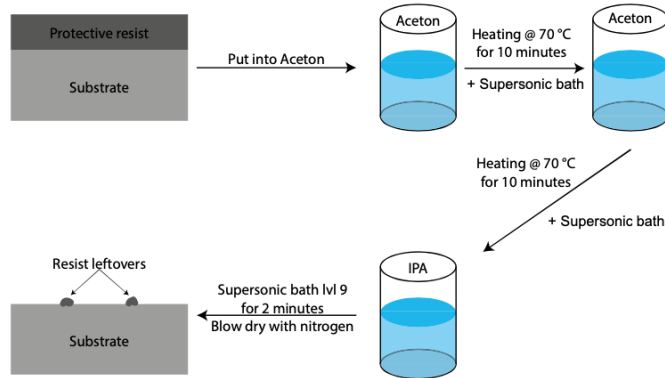


**Figure 3.1:** First cleaning steps to remove the protective resist from the silicon substrate [12].

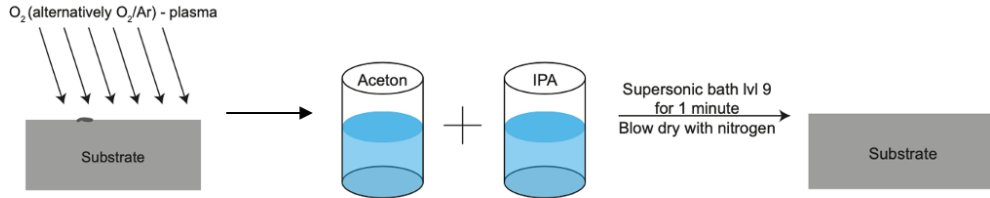


**Figure 3.2:** R.I.E. treatment of the sample to remove potential resist leftovers [12].

### 3.1.2 Spin Coating

The cleaned substrates now undergo spin coating. In this thesis, a double-layer resist system is used for the fabrication of Josephson junction. Since the surface area of the 12 mm × 12 mm exceeds the area of the formerly used 10 mm × 6 mm more than twice (144 mm<sup>2</sup> compared to 60 mm<sup>2</sup>), the volume of the necessary resist for the spin coating has to be optimized during this thesis.

For the bottom resist, the resist 'PMMA/MA33%' is chosen. For the later samples, a volume of 350 µl turned out to lead to good results. After applying it on the substrate, the substrate is rotated at 2000 rpm (rotations per minute) for 120 seconds, afterwards it is baked at 160°C for 10 minutes.

For the second layer, during the first part of the thesis PMMA 950K A2 was used as top resist. Since its properties do not suffice for the implementation of the descum step (explained in Sec. 3.3), the finally used top resist is '950 PMMA A4'. 220 µl of it are rotated at 2000 rpm for 100 seconds and afterwards baked at 160°C for 5 minutes. The relevant difference between the two top resists is that the 950 PMMA

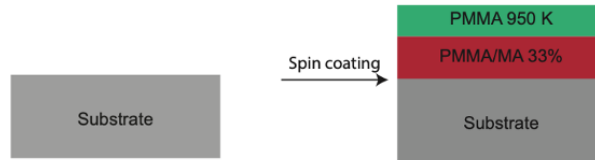


**Figure 3.3:** Schematic illustration of the double-layer resist system [12].

A4 layer is significantly thicker (with approximately 400 nm) than the formerly used PMMA 950K A2 layer (with approximately 200 nm). This increases the stability of the top resist and the Dolan bridge (introduced in Sec. 3.1.3) after the descum is applied on the sample. A schematic illustration of the double-layer resist system can be seen in Fig. 3.3

As last step, gold nanoparticles are put along the edges of the substrate to simplify the focusing during the e-beam lithography.

### 3.1.3 E-beam Lithography

#### Basics of E-beam Lithography

The actual structures are written via e-beam lithography. The resist system contains long polymer chains which are sensitive to high energetic electrons. To break these chains, the beam of a scanning electron microscope (SEM) is utilized. At WMI, this SEM is the NanoBeam nB5 from NanoBeam Limited. The resolution of the electron beam reaches into the nanometer-area, which allows the shaping of structures in the scale of some nanometers.

The actual input for the NanoBeam is a pattern created in a program called 'LayoutEditor', with different layers which each can be written with various charge doses. This again makes an optimization of the e-beam lithography necessary. If the chosen charge dose is too small, the polymer chains of the resist may not be broken properly and the resist will not be completely removed during the development process. On the other hand, a too large charge dose may break too many polymers that should not be written in the immediate vicinity of the actually written areas. This effect is called 'Proximity effect': High energetic electrons are scattered by the resist or back-scattered on the silicon substrate after passing the two resist layers and therefore their energy is deployed into the resist in a wider area around the original entrance point into the resist. An example for the results of the proximity effect on edges compared

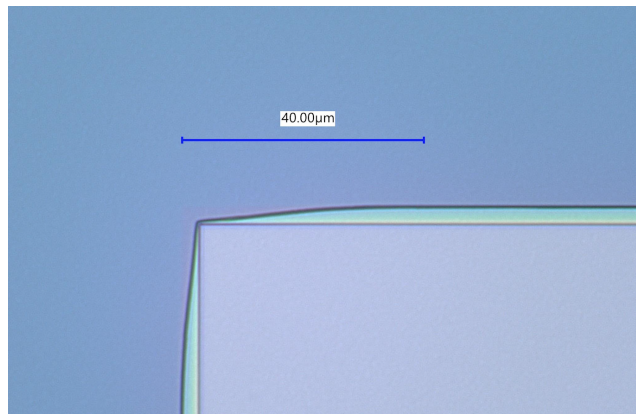


**Figure 3.4:** Optical micrograph of a corner of sample 'JJ12-066-PM'. The resist area, which is affected by the e-beam lithography decreases around the corner of the sample, since the corner is less affected by electron scattering from written resist in immediate vicinity happens.

to corners can be seen in fig3.4.

This proximity effect is also the reason why smaller structures need a higher charge dose than bigger structures: In wide structures, each written point is surrounded by an area, that is also written and therefore the original point receives a significant dose of deployed energy only by the proximity effect of the surrounding area. This is not the case for the small structures of the Josephson junctions, which have a width of 200 nanometers. Hence, the junctions in general receive a much higher charge dose than the wide ground planes, they are connected with.

The reason for the use of a two-layer resist system is the implementation of a so called undercut: Applying a rather small charge dose does not affect the top resist, which is less sensitive to electrons than the bottom resist. The polymer chains of the bottom resist on the other hand are broken. During the development, they are removed from the substrate while the top resist remains. Therefore, we obtain an area, that has no resist on the substrate, but is shielded from above through the intact top resist. This technique is commonly used for the application of shadow evaporation processes.

### E-beam Pattern and Junction Design

The used pattern for the e-beam lithography is adapted various times during this thesis, the here presented pattern is the first one and the one, from where the optimization of the e-beam lithography starts. The pattern consists of 420 SQUIDs with three different SQUID designs. One SQUID design can be found in Fig. 3.5. We

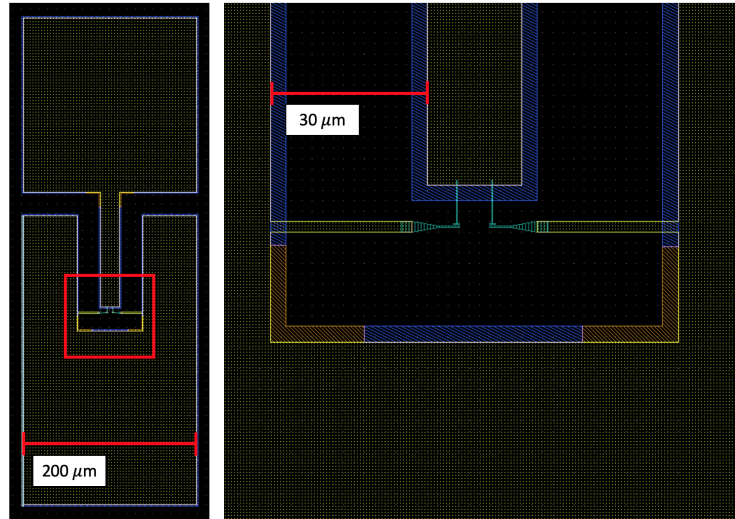


**Figure 3.5:** In the left image, the pattern for a single SQUID can be seen. The big, square shaped structures are the ground planes which are used as contact pads for the resistance measurements. The framed section in the center is the actual SQUID loop and can be seen zoomed in in the right image.

define the two ground planes as the wide, square-shaped structures and the associated structures (yellow dotted in Fig. 3.5). We define the junctions as the actual Josephson junctions, the bridge connecting them with the upper ground plane and rejuvenation of the arms of the two horizontal arms of the ground planes (all three are cyan striped in Fig. 3.5). The ground planes and the junctions are assigned to different layers, so they can be written with different charge doses. During the course of this thesis, two of three designs are removed and replaced by the design from Fig. 3.5. A zoomed in image of the used Josephson junction design can be seen in Fig. 3.6. The here shown Josephson junction is a so called crosstype junction. The structures highlighted in cyan are written with a strong charge dose, such that all of the polymer chains are broken. The green dashed structure that overlaps the junction is written with a weak charge dose to form an undercut in this area. The undercut and the above remaining top resist, that is lying between the two parallel cyan junction parts, is called the 'Dolan bridge' and will be further investigated in Sec. 3.1.5. A schematic illustration of the e-beam lithography and the Dolan bridge can be seen in Fig. 3.7, as well as a mark where in the pattern the schematic writing process is shown.

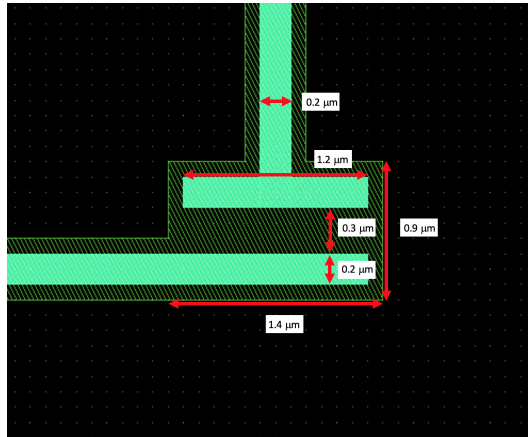


**Figure 3.6:** Crosstype junction pattern. We can clearly see the defined junction area (in cyan) and the undercut (green dashed).

### 3.1.4 Development

When the e-beam lithography is finished, the broken polymer chains have to be removed from the substrate in order to start the evaporation process. Therefore, the written sample is put shortly into a developer which basically removes the resist with the broken polymer chains, and is afterwards dipped into cooled IPA to remove resist leftovers and finish the undercut in a much slower and controlled process, without dissolving the top resist [14]. A schematic illustration can be found in Fig. 3.8

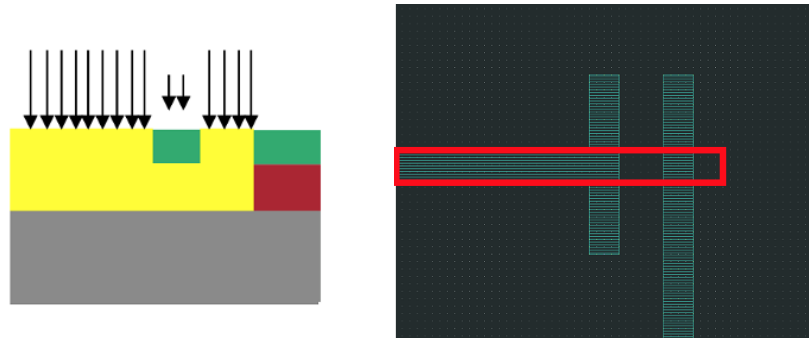


**Figure 3.7:** Left: Schematic illustration of the e-beam lithography in the cross section of the junction area. The yellow area indicates resist with broken polymer chains. The green areas symbolize intact top resist layers, the red areas intact bottom resist layers. The shorter arrows in the center indicate a small charge dose and we can see the undercut with the intact top resist. Right: Location of the cross section in the right image.

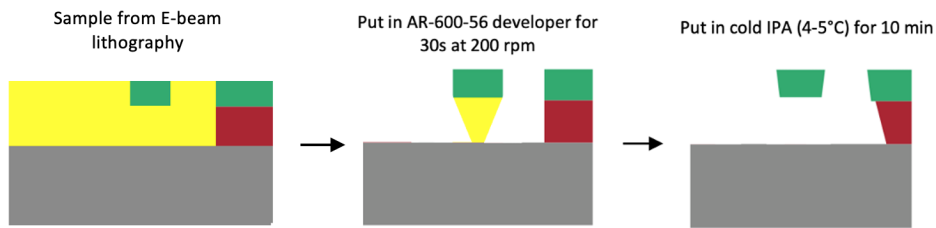


**Figure 3.8:** Schematic illustration of the development process. The yellow area indicates resist with broken polymer chains. The green areas symbolize intact top resist layers, the red areas intact bottom resist layers. The developer is removing most of the resist with the broken polymer chains (central picture), the IPA mainly forms the undercut (right picture).

The used developer is called 'AR-600-56' and the sample is soaked in it for 30 seconds, the IPA is cooled down to 4°C and the sample is put into it for another 10 minutes. In Fig. 3.9 we can see a comparison of a sample that just passed the e-beam lithography and the same sample after the development. The structures where the polymer chains are broken are already clearly visible, and one can see the the silicon substrate after the development process.

### 3.1.5 Evaporation and Oxidation

After the development process, the sample is ready for the evaporation process. For the junctions at WMI (seen in Fig. 3.10), aluminum is used as superconducting material. The evaporation system at WMI allows evaporation of aluminum in vacuum under variable angles. This is necessary, as different evaporation angles are needed for the shadow evaporation. For the realization of Josephson junctions, the developed samples are placed in the evaporation system which gets evacuated. Afterwards, a 40 nm thick layer of aluminum is evaporated onto the substrate at rate of 10 Å/s and an angle of 55° in the way seen in Fig. 3.11. After the first evaporation, an oxidation process at constant pressure in an controlled environment is used to create an uniform AlO<sub>x</sub> insulating barrier. The advantage of the oxidation process in the evaporation chamber is the constant pressure and the lack of contaminations through the atmosphere, for example the absorption of too much water into the oxide barrier. After the oxidation, the second evaporation is started: A 70 nm thick layer of aluminum is evaporated on the substrate at rate of 10 Å/s and an angle of 0°. Therefore, the 'lower section' of the Josephson junction seen in Fig. 3.6 is evap-

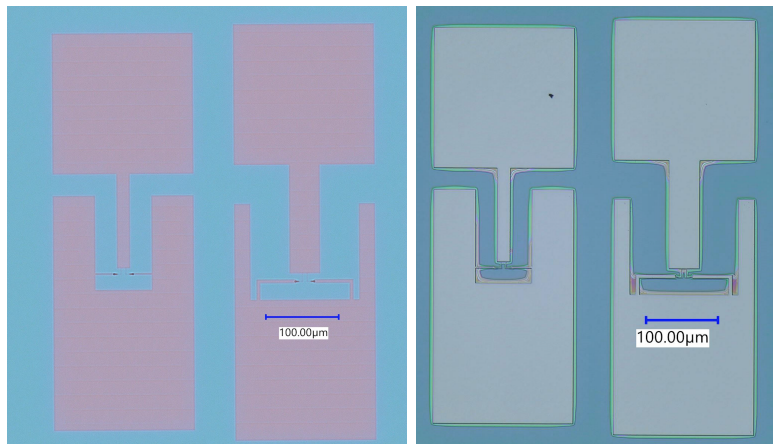


**Figure 3.9:** Optical micrographs of sample 'SQUID12-057-PM' after the e-beam lithography (left) and the development (right). We can see the silicon substrate on the right image, which shows, that the resist layer got removed on the written structures.

orated on top of the 'upper, T-shaped section' of the junction, with the insulating oxide barrier in between. This structure forms the SIS-contact of Fig. 2.1.

After the second evaporation, another oxidation process is utilized to reduce the effects of contamination [17] of the fabricated junctions.

### 3.1.6 Liftoff Process

After the evaporation process, the whole substrate is coated with aluminum. To obtain only the SQUIDs and Josephson junctions, the last step of the fabrication process is the liftoff process. The aluminum coated substrates are put into acetone at 70°C for 1 hour twice and afterwards are put into isopropanol (IPA) at room temperature, which is placed in a weak supersonic bath for one minute. This process slowly removes the resist layers that are still on the substrate and therefore also removes all of the aluminum which is evaporated on top of the resist. Only the aluminum directly evaporated onto the silicon substrate is unaffected by the acetone bath and therefore survives as the only structures of the sample. Fig. 3.12 shows a schematic illustration of the liftoff process, in Fig. 3.13 the finished Josephson junctions can be found, with pictures taken with different microscopes.

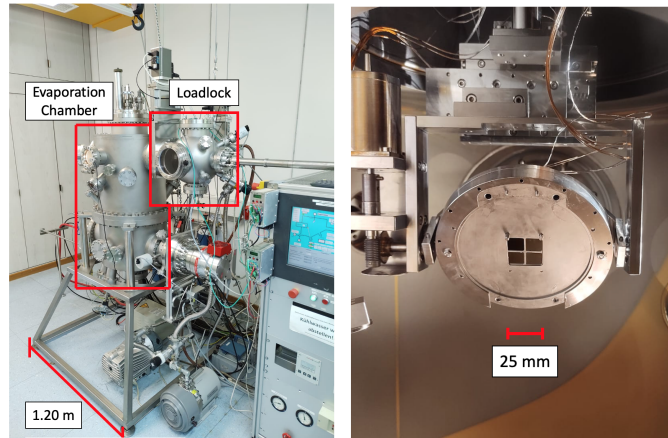


**Figure 3.10:** The evaporation system at WMI. In the left picture, the big cylinder in the back is the evaporation main chamber, the smaller chamber is the load lock for sample transfer. In the right picture, the tilted sample holder during an evaporation process can be seen inside the main chamber.

### 3.2 Measurement of the SQUIDs and Josephson Junctions

In order to gain information about the critical current  $I_c$  of the fabricated Josephson junctions, an evaluation with the microscope is not sufficient to determine more than the intactness of the structures. Henceforth, we have to measure the resistance of the Josephson junctions and calculate the critical current via Eq. 2.7. Hence, a current voltage characteristic for each SQUID is recorded to evaluate the resistance and therefore the critical current.

For that purpose, two contact needles held by a wafer probing station are connected with a source meter, which sweeps through a given voltage range and records the current across the junctions. The sample with the different SQUIDs is placed under a microscope as well as the contact needles and we can set the needles on both contact pads of the structure. Hereby, much care has to be taken such that the needles do not deeply scratch into the aluminum film and tap the silicon substrate underneath, but touch the metal surface gently. After a full sweep of the voltage, we can rearrange the needles for the next measurement. An example for a recorded U-I-characteristic can be seen in Fig. 3.15. The voltage sweep ranges from -1 mV to +1 mV to avoid a possible burn of junctions caused by too high current flows. Since all measurements are recorded at room temperature, always an ohmic resistance in the  $k\Omega$  range of the is recorded for the junctions.

The U-I-characteristics are saved and are evaluated by a python script written by

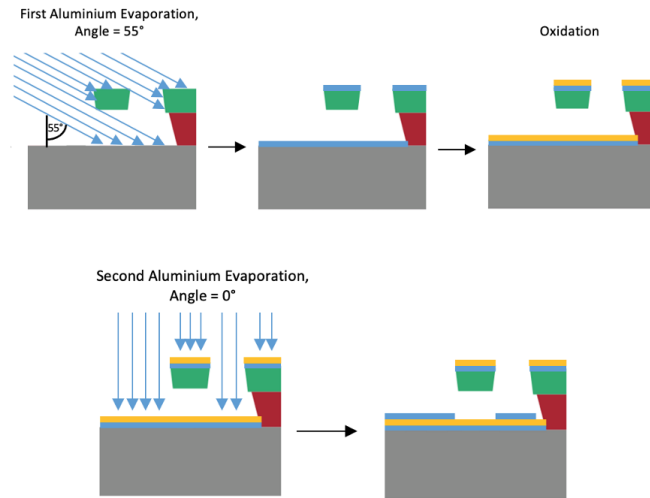


**Figure 3.11:** Schematic illustration of the evaporation process. The cross section of the scheme is the same as in Fig. 3.7. The evaporated aluminum layers are depicted in light blue, the AlO<sub>x</sub> barrier are depicted in orange.

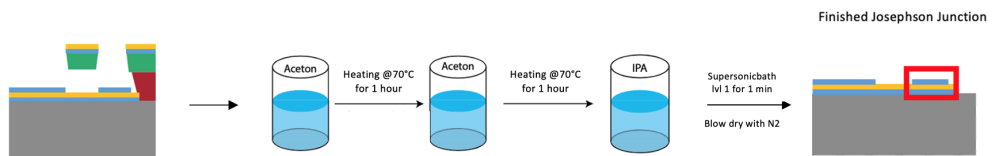


**Figure 3.12:** Schematic illustration of the liftoff process. The red box highlights the actual Josephson junction. The aluminum layers are depicted in light blue, the AlO<sub>x</sub> barrier are depicted in orange.

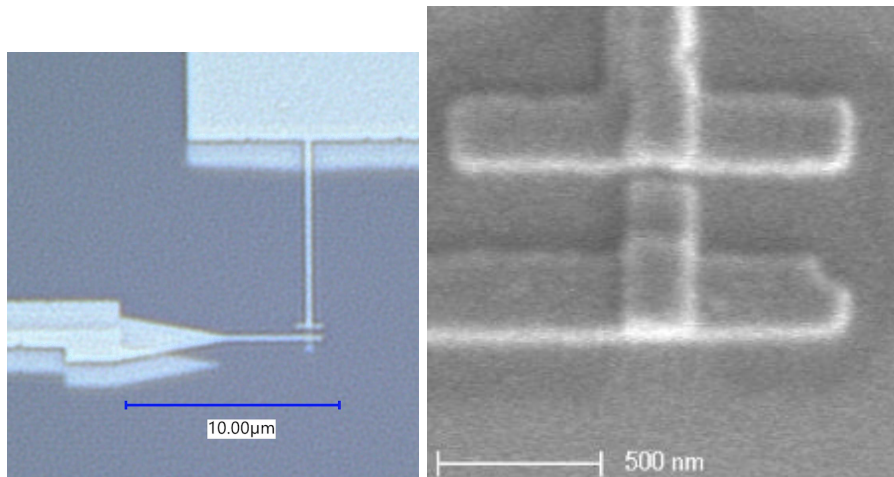


**Figure 3.13:** Images of a crosstype junction. Left: Optical micrograph of a intact junction. Right: SEM-Image of a junction fabricated and recorded by Christoph Scheuer [12].

Christoph Scheuer [12] and that was adapted in this thesis. The mean resistance is calculated out of the U-I-characteristic and plotted against the position on the sample. Also, the critical current can be calculated with Eq. (2.7) and the critical current density  $J_c$  can be calculated, if the junction area is measured with suitable microscopes like a SEM.

An image of the wafer probe station can be seen in Fig. 3.14

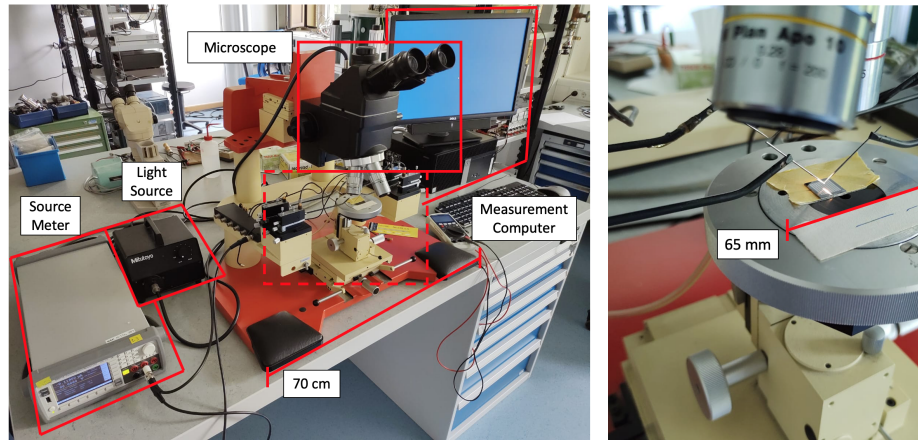


**Figure 3.14:** The wafer probing station at WMI. On the left picture can be seen: A source meter to record the U-I-characteristics, a light source for the microscope and the computer for recordings of the measurements. The actual probing station with the measurement contacts above the sample holder can be seen in the dashed box. A zoomed in image of it can be seen in the right, with a SQUID currently being measured.

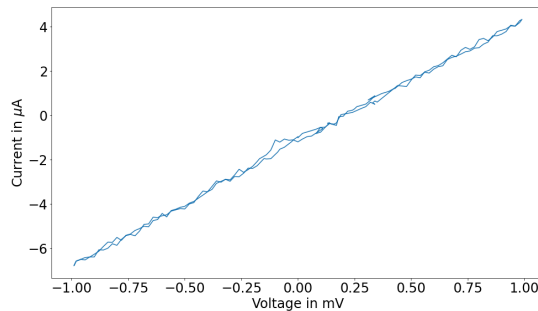


**Figure 3.15:** Recorded U-I-characteristic of one SQUID of SQUID12-057-PM. The ohmic behaviour can be clearly seen.

### 3.3 The Descum Step

In this thesis, another fabrication step, the descumming, will be examined with regard to its efficiency. The descumming is done after the development process and before the evaporation. The descum process removes resist residues in the developed areas of the sample [18], which is desirable to reduce losses through two level systems. For the descumming, the PLASSYS system at WMI is used. An image of

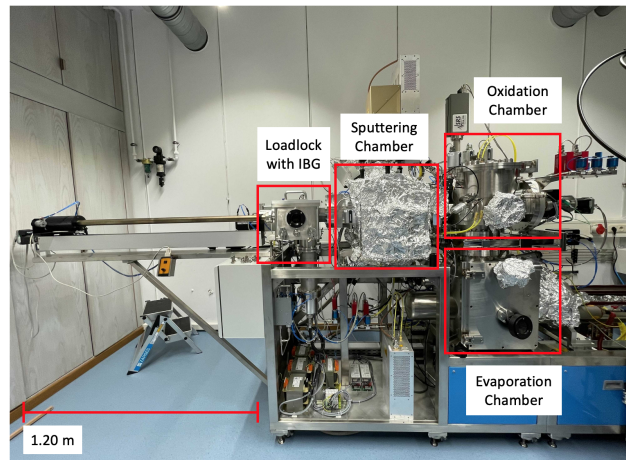


**Figure 3.16:** The PLASSYS system at WMI. The ion beam gun for the descumming is located inside the load lock.

PLASSYS can be seen in Fig. 3.16. With its ion beam gun (IBG) an ionized beam of argon and oxygen is accelerated onto the sample for a given time. This argon-oxygen-plasma further removes resist residues that were not removed through the development process.

To evaluate the effectiveness of the descumming, the room temperature resistance of the SQUIDS is measured after the liftoff process, then the samples will be thermally annealed, which means heating at a high temperature for a given time, and after the annealing they are measured again. As described in [17], thermal annealing in general accelerates the aging process of Josephson junctions, in which unwanted molecules are absorbed into the  $\text{AlO}_x$ -layer, which therefore 'grows': It increases in height. Since the oxide layer serves as the insulating barrier of the Josephson junction, an increase in the junction resistance can be measured. This resistance increase is reduced significantly when applying plasma cleaning on the samples [19] and leads to the conclusion, that the growth of the oxide barrier is dependent on resist leftovers on the substrate, which are absorbed into the barrier during the annealing process. The effectiveness of the descum process therefore can be evaluated via the measurement of the resistance increase of the Josephson junctions after the annealing process.

# Chapter 4

## Experimental Results

### 4.1 Optimization of the E-Beam Charge Dose

#### 4.1.1 Optimization of the Double-Layer Resist System PMMA/MA33 and PMMA 950K A2

The first part of this thesis is about optimizing the fabrication steps mentioned in Secs. 3.1.1 - 3.1.6. Since the silicon substrate changes from the previously used  $10 \text{ mm} \times 6 \text{ mm}$  to larger  $12 \text{ mm} \times 12 \text{ mm}$  chips, beginning from the spin coating most of the subsequent steps have to be adjusted concerning the used parameters. In detail, this means adjusting the volume of resist used in the spin coating, finding the optimal charge dose for the e-beam lithography for the adapted resist system and optimizing the development process is necessary in order to fabricate reproducible and uniform structures for analyzations of the descum step.

As for the spin coating, the amount of the used bottom and top resist are both increased in the first sample series, since the area of the bigger samples is more than twice the area of the formerly used ones. On the other hand, most of the liquid resist is thrown off the substrate by centrifugal outflow at the beginning of the spin coating [13] which leads to the consideration, that no or not a too big increase of the resist volume may be necessary.

Each fabrication series consists of four samples, which are fabricated at the same time. For the first fabrication series, the resist volume is chosen differently on each of the four samples to observe possible effects of the different resist volumes. Those reached from  $440 \text{ }\mu\text{l}$  bottom resist and  $220 \text{ }\mu\text{l}$  top resist to  $560 \text{ }\mu\text{l}$  bottom resist and  $280 \text{ }\mu\text{l}$  top resist. The acceleration time, the rotations per minute and the baking time are not changed, all parameters can be found in the appendix.

To save time and material, the samples with different spin coating parameters are written with an e-beam pattern with varying charge dose. Since the ground planes of the SQUIDs are additionally written with a different charge dose than the Josephson junctions, the individual optimal charge doses for the ground planes and the junctions



**Figure 4.1:** Early SQUID pattern in layout editor. The different colours of each column of the SQUID-triplets indicate different charge dose doses for the ground planes, the blue numbered boxes indicate different charge doses for the Josephson junctions

can be determined simultaneously. In Fig. 4.1 the pattern used to determine the optimal charge doses can be seen. The layers and therefore the charge dose for the ground planes are different for each column, with the lowest charge dose on the first column on the left, and the highest charge dose on the column on the right. The charge dose for the Josephson junctions is varied within clusters of ten SQUID-triplets in the way we can observe in Fig. 4.1. This distribution gives the charge dose variation of the junctions some independence from the charge dose variations of the ground planes and allows statements about the quality of the junctions and the ground planes separately.

As for the first fabricated SQUIDs, after the development we see resist leftovers across the whole ground planes of the SQUIDs with the optical microscope. The amount of resist leftovers does not vary with the different volumes of resist used on the four samples of one series, but shows a clear dependency of the charge dose within one sample: The SQUIDs written with the lowest charge dose of the samples have way more leftovers on them than the SQUIDs written with the highest charge dose, as can be observed in Fig. 4.2. Another consideration is the adaption of the development process. The process so far just leaves the sample lying in the developer for 30 seconds, in order to achieve a reproducible process independent of the executing person, for example through different techniques of stirring or shaking the sample in the remover. Without any motion at all on the other hand, broken polymer chains may remain on the samples, because there is no flow of the surrounding liquid. Therefore the developer is stirred with a magnetic stirrer and the sample is dipped

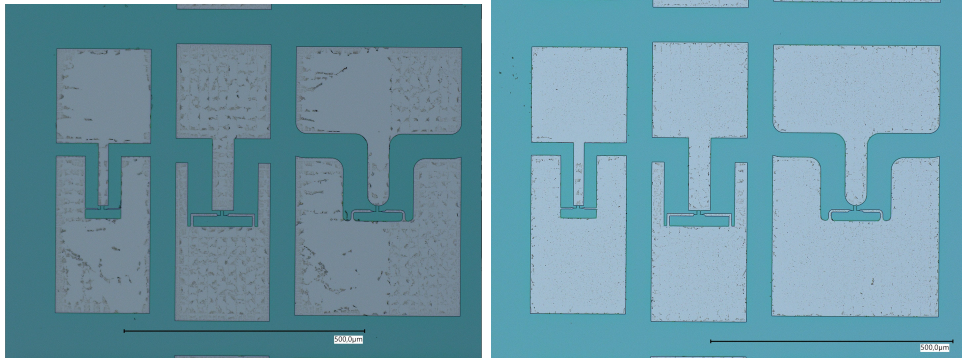


**Figure 4.2:** Optical micrographs of two SQUID-triplets of sample 'SQUID12-046-PM'. The ground planes in the left picture are written with a charge dose of  $6.0 \text{ C/m}^2$ , the structures in the right picture with a charge dose of  $6.9 \text{ C/m}^2$ . The decrease of resist leftovers with the increase of the charge dose can clearly be seen.

in the liquid, with the written structures facing down towards the bottom of the beaker. This adaption of the development process yields a significant decrease of resist leftovers as can be observed in Fig. 4.3 and still keeps the process highly independent from the fabricating person. Sample 'SQUID12-047-PM' is written with the same charge doses as sample 'SQUID12-046-PM' in Fig. 4.2, the only difference is the stirring of the developer.

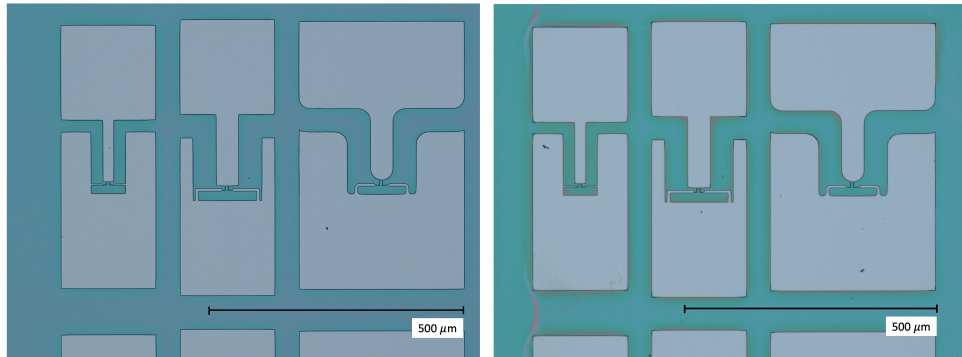


**Figure 4.3:** Optical micrographs of two SQUID-triplets of sample 'SQUID12-047-PM'. The ground planes on the left picture are written with a charge dose of  $6.0 \text{ C/m}^2$ , the structures in the right picture with a charge dose of  $6.9 \text{ C/m}^2$ . The decrease of the resist leftovers through the stirring of the rotation of the developer can be clearly seen.

### 4.1.2 Optimization of the Double-Layer Resist System PMMA/MA33 and 950 PMMA A4

The implementation of the descumming step into the fabrication process is the main goal for this thesis. The so far used double-layer resist system consisting of a bottom layer with a thickness around 650 nm and a top layer with a thickness up to 100 nm [12]. The probability for the Dolan bridge to survive the fabrication until the evaporation process will decrease through the descumming step, since it removes a specific amount of resist via argon-oxygen-plasma. To solve this problem, a new top resist has to be implemented, which has already been investigated [18] and which is from now on adopted into the fabrication process. The bottom resist does not change, but for the top resist now '950 PMMA A4' is used. The use of this resist at the KIT resulted in a double layer resist system, with a significantly thicker top resist with approximately 350 nm [18], which increases the chance of survival of the Dolan bridge.

Since the resist system now has significantly different properties regarding the e-beam lithography, the optimal charge dose has to be evaluated again. Since the top resist layer now is significantly thicker than in the old resist system, the charge dose is increased from the formerly  $6.0 \text{ C/m}^2$  -  $6.9 \text{ C/m}^2$  up to  $9.0 \text{ C/m}^2$  -  $10.8 \text{ C/m}^2$ . With these charge doses, still resist leftovers can be seen on the developed sample 'SQUID12-056-PM' shown in Fig. 4.4 and the junctions are not developed at all. Therefore the charge dose is increased up to a range of  $11.2 \text{ C/m}^2$  -  $13.0 \text{ C/m}^2$  on the sample 'SQUID12-057-PM', which shows much better developed structures as can be seen in Fig. 4.5.

What also can be found, is the wide undercut of sample 'SQUID12-057-PM'. Since

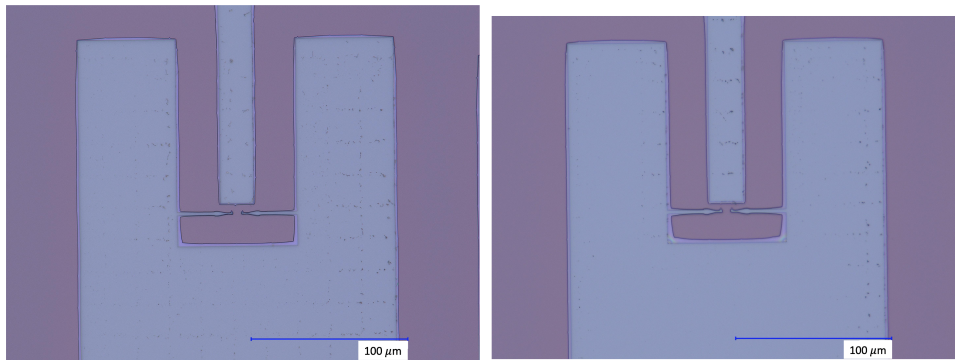


**Figure 4.4:** Optical micrographs of two SQUIDs of sample 'SQUID12-056-PM'. The ground planes on the left picture are written with a charge dose of  $9.0 \text{ C/m}^2$ , the structures in the right picture with a charge dose of  $10.8 \text{ C/m}^2$ . Even with the higher charge dose, resist leftovers are visible and the junction is not developed.

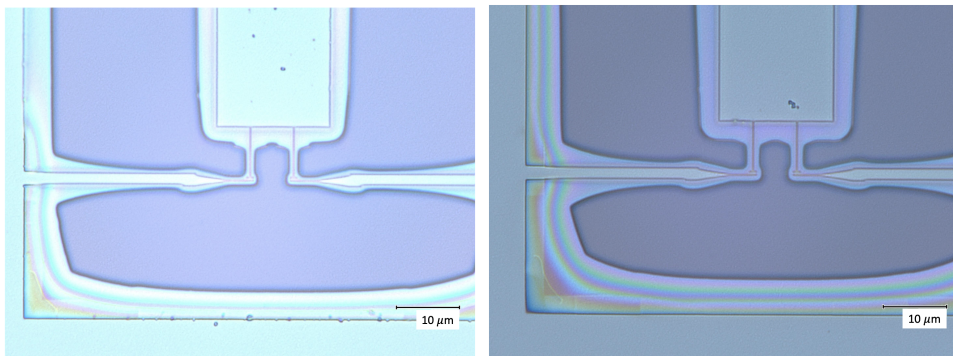


**Figure 4.5:** Zoomed in micrographs of the junction area of two SQUIDs of sample 'SQUID12-057-PM'. The ground planes on the left picture are written with a charge dose of  $11.2 \text{ C/m}^2$ , the structures in the right image with a charge dose of  $13.0 \text{ C/m}^2$ . In the right image, the edges are well developed and barely any resist leftovers can be seen. In both images the junctions look well developed.

the charge dose is relatively high (up to  $13.0 \text{ C/m}^2$ ), the proximity effect could possibly affect the edges of the structures in a negative way. Therefore, an extra layer is added to the e-beam pattern, which surrounds the whole ground planes and is written with a small charge dose. This layer only affects the bottom resist but leaves the top resist mostly intact, in order to weaken the proximity effect in direct vicinity to the edges of the SQUID. Since the top resist remains intact, no aluminum is evaporated onto unwanted areas of the silicon substrate. This solution is not perfect, since the descum step could remove the surviving top resist and expose the silicon substrate to the aluminum evaporation.

A solution for this problem is the during the course of this thesis purchased BEAMER-software [20]. BEAMER takes an e-beam pattern as input and simulates an e-beam lithography process, in which it calculates the proximity effect on each point of the pattern and fractures it into many different layers with an assigned relative dose compared to the other layers. This fracturing happens in a way, that the structures are written with an optimal dose with the environment staying as unaffected as possible.

An example for a SQUID-pattern before and after the proximity effect correction (PEC) can be seen in Fig. 4.6.

Since BEAMER only creates a dose table with relative values of the charge doses to each other, one reference dose still has to be determined. Therefore, the ground planes are set as reference layer. In the nano pattern file (npf), the multiplication factor for this reference dose - also called 'relative charge dose' - is 1. For the determination of the optimal charge dose for the ground planes, samples without the application of BEAMER are used. In specific, sample 'SQUID12-057-PM' is used,

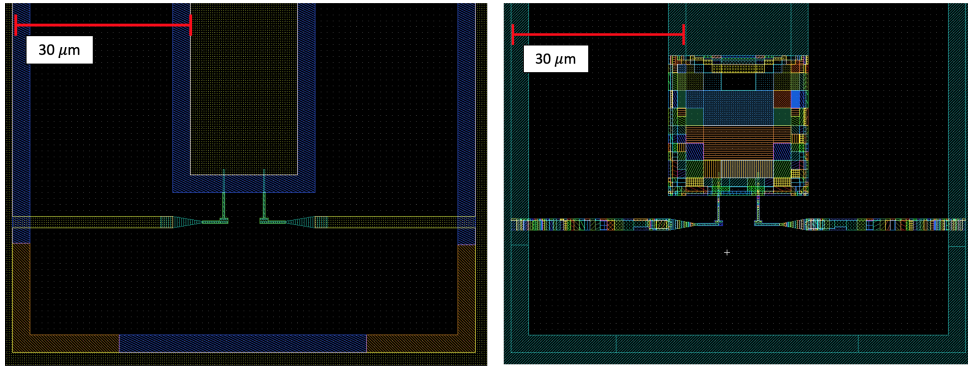


**Figure 4.6:** E-beam patterns with (right) and without (left) proximity effect correction (PEC) by BEAMER. The blue and brown surroundings from the uncorrected pattern are merged with the big ground plane layer to the reference layer. The structures around the junctions are fractured into different layers by BEAMER and get assigned different charge doses.

since the developed structures (Fig. 4.5) look promising. The aluminium structures after the evaporation, oxidation and liftoff steps can be seen in Fig. 4.7.

Since the junctions look well defined with the optical microscope, the current

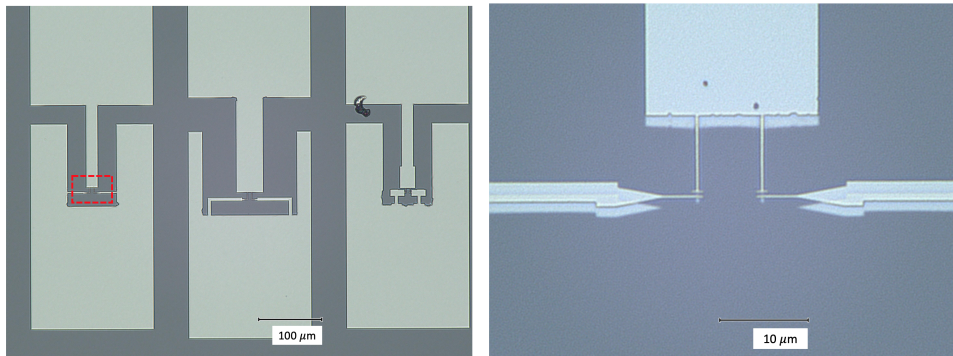


**Figure 4.7:** SQUIDs of sample 'SQUID12-057-PM' after liftoff. On the left image we can observe an overview of the SQUID-triplet. On the right image, a zoom into the red framed junction area of the left SQUID can be seen. The two offset aluminum layers of the shadow evaporation can also be seen.

voltage characteristics are measured at the probing station. Calculating the room temperature resistance of the SQUIDs and plotting the result against the position on the chip results in the plot shown in Fig. 4.8. The optimal charge dose is meant to be the charge dose, where the SQUID resistance is as constant and uniform as possible, since the goal of an optimized fabrication process is a uniform final product. Looking for the columns with the most uniform resistance, the best results

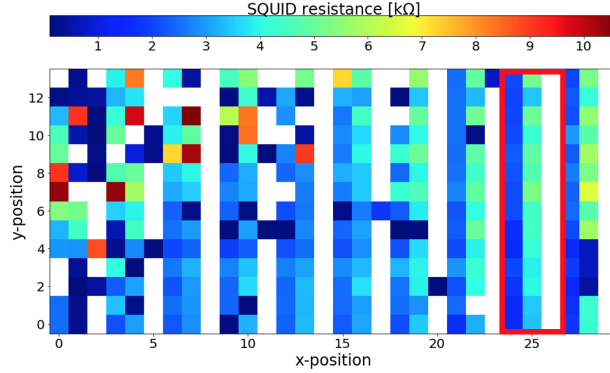


**Figure 4.8:** SQUID-resistances of sample 'SQUID12-057-PM'. Three columns together equal one SQUID-triplet. Each SQUID-triplet is written with a different charge dose. Every third column is coloured nearly completely white, since the used SQUID-design is designed for lower charge doses and therefore results in a short-circuited aluminium structure. Column 9 has the most uniform junction resistance and is framed red.

are found in the last three columns, in specific in column 9 (framed red in Fig. 4.8), which equals a charge dose of  $12.8 \text{ C/m}^2$  on the ground planes. Hence, this value is taken as the reference charge dose for the PEC pattern, which is used for the further fabrication.

### 4.1.3 Optimized Single Junction Pattern

To get a more accurate measurement of the Josephson junctions, the formerly used SQUID pattern is now reduced to a single junction pattern. In the formerly used SQUID pattern, variations of the junction properties cannot be extracted clearly through the resistance measurements. For example, when a higher resistance of the SQUID compared to the mean value of other SQUIDs is measured, this could be two junctions with a significantly smaller junction area or a slightly thicker  $\text{AlO}_x$  barrier. On the other hand, this could also be two junctions with good properties, where the bridge, which normally connects the junction with the big ground planes, is broken for one junction and therefore only one junction is remaining. Through the use of a pattern with only one Josephson junction connecting the two aluminium ground planes, we can directly recognize junctions with deviating properties. Since the optimal charge dose is determined, the e-beam pattern with varying charge doses for each junction-triplet is replaced by a pattern with the same charge doses for every junction.

Additionally, in the first, sixth and eleventh row of the pattern short circuited alum-

num structures are implemented. Since the measured resistance of the Josephson junctions is not completely attributable to the junction resistance, but also has a small part which can be attributed to the ohmic resistance of the overall aluminum structures, subtracting the mean value of the short circuited structures allows a more precise calculation of the resistance of the junctions than before. To measure the resistance that fits the layout of the junctions and ground planes best, the actual layout is copied and only the junction itself is shorted, as can be seen in Fig. 4.9. The optimal pattern also already includes the proximity effect correction (PEC) by BEAMER. To avoid position deviations of the NanoBeam during its writing process, the ground planes and the PEC-areas are written in a single writing process, and the PEC-junctions are written in an extra writing process. Therefore, even though some charge doses of the ground planes may match with those in the junction region, those two structures are moved to entirely different layers to enable individual lithography. This also brings the advantage, that the junctions can be written with a significantly lower beam current than the ground planes, which increases the quality of the smaller structures even more. In the appendix, the relative doses of each layer can be found.

To be able to evaluate the effects of the PEC, the formerly used SQUID-triplets with



**Figure 4.9:** Short circuited ground planes. The structure equals the normal junction structures, only the Josephson junction itself is removed and a direct aluminium bridge is inserted.

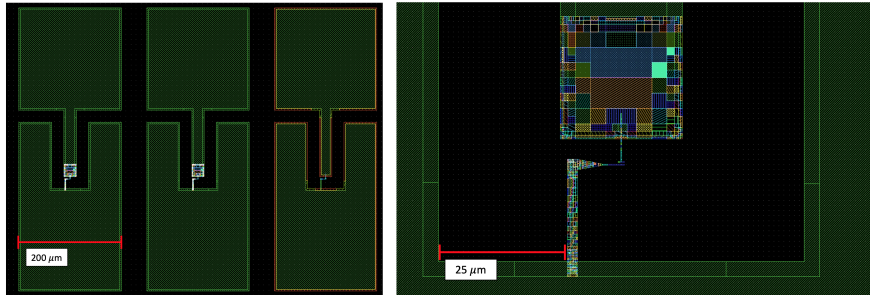


**Figure 4.10:** Section of the optimized single junction pattern. On the left one junction triplet can be seen, with PEC in the left and middle junction and one uncorrected comparative junction on the left. In the right image a zoom of the junction area itself can be seen, as well as the fractured pattern due to the PEC. Only the junction and a square-shaped area of the ground plane receive PEC.

different designs of each SQUID are now changed to three identical ground planes connected via single junctions, where the first two of them received the PEC and the last one stayed uncorrected as comparative junction. In Fig. 4.10 one junction triplet of the final single junction pattern can be seen. In Fig. 4.11 one example for the resulting junctions can be seen on sample 'JJ12-064-PM'. Overall, on the samples created with the optimized pattern the junctions look well defined and uniform. The only flaw is the PEC area of the ground plane lying above the junctions, where comparatively many resist leftovers can be seen. Where the junctions are well defined, the charge dose for this area seems to be still too small. However, The more important junctions are free of the resist leftovers, therefore we move to the implementation of the descum step.

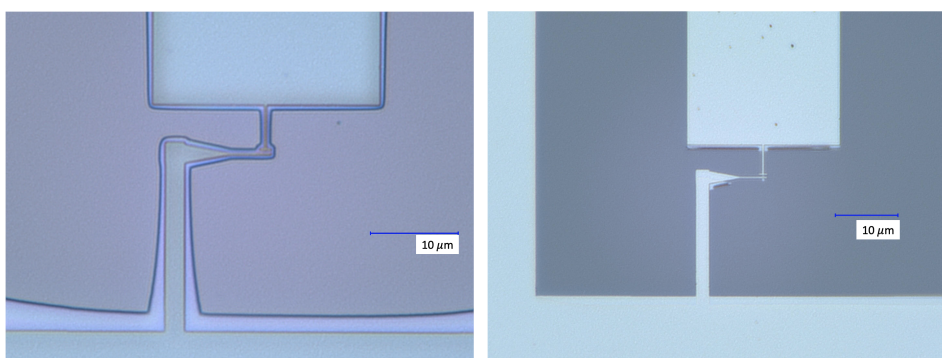


**Figure 4.11:** Josephson junctions of sample 'JJ12-064-PM' after development (left) and after liftoff (right). The junction is well defined, only on the ground plane on the top resist residues can be seen, the PEC area of the ground plane seems to use a too small charge dose.

## 4.2 Implementation of the Descum Step

### 4.2.1 Realization of a Stable Plasma Beam at PLASSYS

As already mentioned in Sec. 3.3, the descumming step is added to the fabrication process between the development process and the evaporation, to reduce potentially remaining resist leftovers from the developed areas of the sample, in order to remove sources of decoherence as two level systems in the resulting samples.

Since the descumming at the new PLASSYS system has to be implemented at WMI for the first time, some tests of the parameter space of the Ion Beam Gun (IBG) are necessary as a first step. The possible tunable parameters for the IBG are: The argon/oxygen plasma flow, the discharge voltage, the beam voltage and current, the

acceleration voltage and the time, how long the shutter for the plasma flow will remain open. The ignition of the argon/oxygen plasma is controlled by the discharge voltage, a minimal value of 40 V is recommended by the manufacturer. The beam voltage and current shape a plasma beam out of the ionized argon/oxygen plasma and control the plasma current. The acceleration voltage sets the level the plasma beam is accelerated on the sample for the descumming.

For the first runs we try to set up a stable beam with the parameters used at KIT with the same PLASSYS system [18]. Parameter values can be found in Tab. 4.1. However, these values do not lead to a stable beam: When setting the parameters, starting the gas flow and igniting the plasma, after around 30 seconds the plasma beam dies off and an error occurs. Repeating this process and varying the parameters slightly in either direction does not result in a stable plasma beam. Therefore, systematic variation of the parameter space is necessary, concentrating on the three parameters: beam voltage, beam current and acceleration voltage. The discharge voltage and the plasma gas flow are mostly kept at their values, since the plasma ignition has already been working and the gas flow as the most important parameter for the descumming has been successfully used at KIT.

Parameter variation shows, that the three previously mentioned parameters are highly dependent of each other: A too high beam voltage prohibits a low beam current, the beam current on the other hand defines a certain range for the acceleration voltage in which a stable beam can be sustained. Exceeding or falling below these values for the acceleration voltage again leads to the beam dying off after some seconds. In detail, the results of the parameter variation yields the following results:

- The beam voltage defines the lower bound for the beam current. For a beam voltage of 400 V, no stable beam with a current of 20 mA or below can be established. For a voltage of 300 V, no beam with a current of 17 mA or below can be established and for a voltage of 200 V, no current of 15 mA or below can be established. The beam current of 10 mA used at KIT can not be realised in a stable beam.
- Setting the Oxygen flow to zero, resulting in a gas flow of  $\text{Ar}/\text{O}_2 = 5/0$  allows the setup of stable beams with much lower beam currents, compared to plasma beams with a gas flow of  $\text{Ar}/\text{O}_2 = 5/10$ . Those beams, however, are not desired for the descum recipe.
- Setting up a stable beam and fixating the parameters beam voltage and current allows for comparatively wide variation of the acceleration voltage. For example, for a beam with a beam voltage of 400 V and a beam current of 40 V, stable beams are set up with acceleration voltages reaching from 110 V to 220 V. For a beam with a beam voltage of 200 V and a beam current of 20 V,

	KIT	Test 1	Test 2
Ar/O <sub>2</sub> flow [sccm]	5/10	5/10	5/10
Discharge voltage	40 V	40 V	40 V
Beam voltage	200 V	400 V	200 V
Beam current	10 mA	40 mA	20 mA
Acceleration Voltage	110 V	220 V	110 V

**Table 4.1:** Values for different parameters of the plasma beam used for descumming with the IBG at PLASSYS. The left column shows the values used at KIT [18], the columns labelled with 'test' are mentioned in Sec. 4.2.2.

stable beams are set up with acceleration voltages reaching from 60 V to 110 V.

#### 4.2.2 Testing the Descum Potential of the IBG

After a stable plasma beam for the descumming is set up, the descumming potential on the samples and their resist system needs to be tested to avoid too strong or too weak descumming. Therefore, sample 'JJ12-063-PM' is used as a test sample for the IBG. The sample is fabricated after the previously optimized fabrication process. Like on the other samples, the PEC area of the ground plane shows some visible resist leftovers. Those, however, prove pretty valuable for the evaluation of the descumming potential on resist leftovers, since the effects on potential leftovers can be measured directly on those existing leftovers.

To measure the effects of the descumming, measurements with an atomic force microscope (AFM) are done before and after the application of the descumming. The AFM image of the sample before the first descumming can be found in Fig. 4.12. For the determination of the resist height, the height differences between the substrate surface and the resist surface are measured across the line seen in Fig. 4.12 and the average height difference is taken as resist height. For sample 'JJ12-063-PM', this leads to a resist height of 861 nm before the descumming.

As a first test, the parameters for the plasma beam are set comparatively high, since it is unclear how strong the descum effects will be in the end. The parameters for the test runs can be found in Tab. 4.1. The plasma beam is accelerated onto the sample for 60 seconds. After the descumming, another AFM image of the same area of the sample is recorded. The measured height now is 780 nm, therefore roughly 80 nm of the resist is removed through the descumming.

For the second test, the parameters of the beam voltage, current and the acceleration voltage are reduced compared to the first test, therefore they match the values the KIT uses for their descumming processes except for the beam current. AFM images

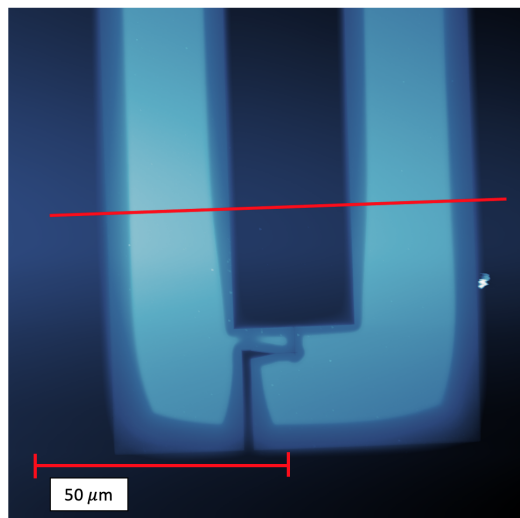


**Figure 4.12:** AFM image of sample 'JJ12-063-PM' before the application of the first descumming. The dark regions symbolize lower located regions and therefore developed areas, the brighter parts symbolize higher located regions and therefore the not written remaining resist. The red line in the center indicates the area used for the measurement of the resist height.

after the descumming result in a resist height of 733 nm, therefore roughly 40 nm of the resist is removed.

Since the height measurements only address the wide top resist layer, further validation is needed that small resist leftovers are removed in a similar way as the resist layer. Therefore, the square-shaped PEC area of the ground plane, which can be observed in Fig. 4.10 and which shows visible resist leftovers (for example seen in Fig. 4.11) are analyzed in detail. Using auto-thresholding methods, the resist leftovers are distinguished from the background and their height in relation to the background is determined. The images of the detected resist leftovers before and after the first descum test can be seen in Fig. 4.13 together with the count rate of the leftovers against their height.

The measurements, especially the plots of the resist leftover counts and their height clearly show a decrease of the height of the leftovers. Comparing the height distribution of the two plots in Fig. 4.13, we recognize that the curve is shifted nearly linearly by approximately 70 nm in height to the left after the descumming, since the local minimum and the distribution around it stay the same before and after the descumming. The measured leftovers with heights of 50 and 60 nm before the descumming cannot be distinguished from the background of the image after the descumming anymore and are therefore no longer recognized in the plots, which underlines this statement. Comparing the decrease of 70 nm of the resist leftovers height with the

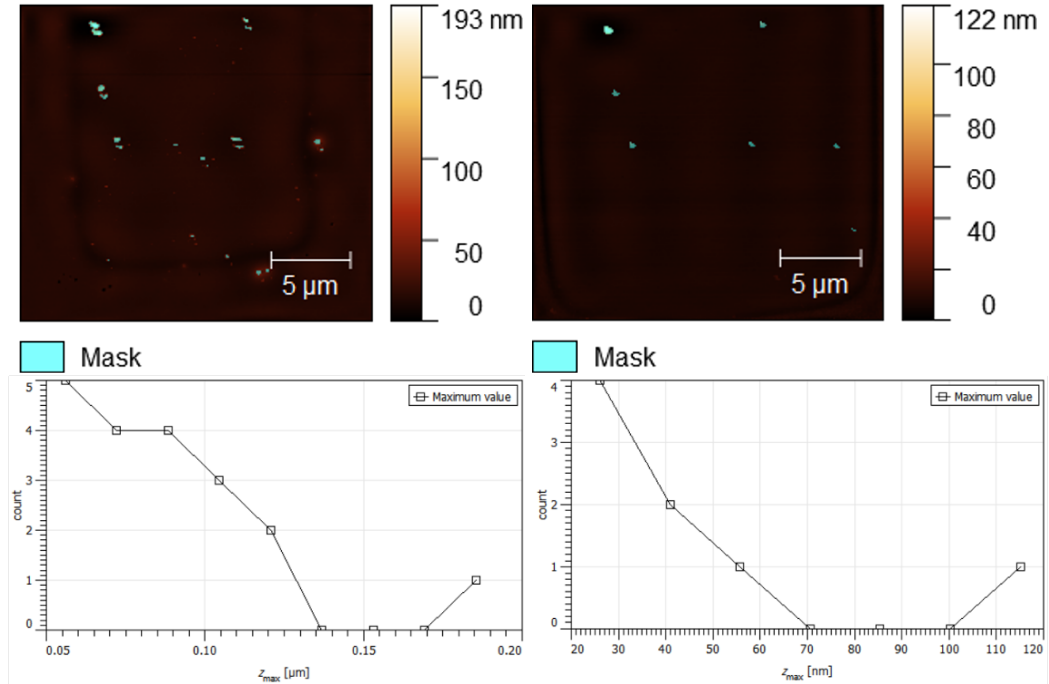


**Figure 4.13:** AFM images and evaluation of the PEC area of the ground plane of sample 'JJ12-063-PM'. In the upper pictures, the resist leftovers are highlighted as a mask in blue for the sample before (left) and after (right) the descumming using an auto-thresholding function. In the lower pictures the counted resist leftovers of the mask before (left) and after (right) the descumming are plotted against the measured height.

decrease of 80 nm of the resist layers height, we can make statements about the effectiveness of the removal of resist leftovers only through the measurement of the removal of the general resist layer.

Similar measurements of the height decrease of the resist leftovers for the second descum test cannot be made, since the AFM images of the second test are blurred in the PEC area of the ground plane. Still, after combining these results especially the second test seems reasonable for the integration into the fabrication process, since the removal of 40 nm of resist should not affect the stability of the Dolan bridge and the removal of 40 nm of resist leftovers already should show an improvement of the sample quality.

### 4.2.3 Measurement of the Descumming Effect

Before any sample is being descummed, a test sample without the descumming step is being fabricated, measured, annealed and measured again after the annealing process, to get a first impression if the annealing does show an effect with the chosen temperature. A python script calculates the relative resistance decrease due to the annealing. For the annealing, the test sample 'JJ12-062-PM' is put on a heating plate in the clean room at 200 °C for 5 minutes. The results of the measurement can be found in Fig. 4.14. For the relevant measurement of the PEC junctions, a resistance decrease of 27.77% is measured.

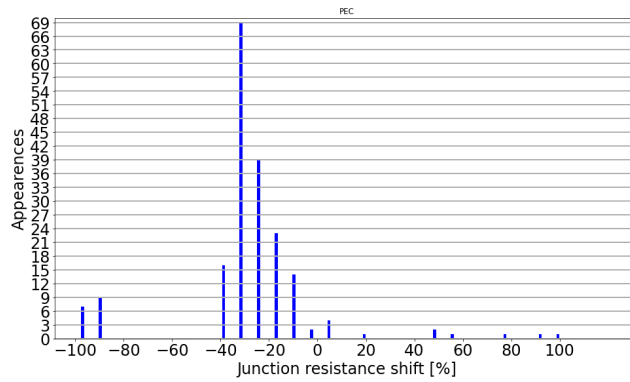


**Figure 4.14:** Relative resistance change for the PEC-junctions of sample 'JJ12-062-PM'. The tendency of a resistance decrease is clearly visible. More detailed plots can be found in Appendix A.1

Unexpectedly, we measure a resistance decrease for the Josephson junctions, instead of the resistance increase, which should give hints about the effectiveness of the descumming. This measurement result, however, is in agreement with other experiments with the resistance reduction of 20-50% [19][21][22][23]. There is no microscopic theory which explains the resistance decrease, yet there are two explanations for this behaviour. In both, the resistance decrease is attributable to a reduction of the  $\text{AlO}_x$  barrier thickness of the junction. The first reason for this could be the formation of aluminum hydroxides [19] in the presence of water molecules in the atmosphere during the annealing. The aluminum hydroxides vary in crystalline structure [21] and the barrier thickness is reduced, due to an overall increase of crystalline phases compared to the barrier composition before the annealing and the overall more dense stacking of crystalline structures compared to amorphous structures. The second reason for the barrier thickness reduction takes a similar approach. Due to the annealing, defects in the  $\text{AlO}_x$  layer are annihilated and initially amorphous  $\text{AlO}_x$  layers re-crystallize,

this structural ordering decreases the barrier thickness [23].

With those explanations, the fabrication process is slightly adapted, to avoid the resistance reduction for the descummed samples. After the sample evaporation and oxidation, the samples are kept in vacuum conditions as long as possible and are only at atmosphere for the resistance measurements and transfers between different stations, for example the probe station and the desiccator, where the sample is kept in vacuum. Additionally, the samples are not annealed on a hotplate in the clean room anymore, but rather are annealed in the 'SUPERBOWL' at WMI, which allows annealing at near-vacuum conditions. Those adaptations are done, to possibly avoid the absorption of water into the  $\text{AlO}_x$  layer of the junctions and therefore to reduce or remove the resistance reduction. Also, a resistance increase can be measured in other experiments after the annealing in vacuum [17], which makes this approach even more promising.

With this adapted fabrication process, multiple different samples are prepared until after the development for the measurement of the effect of the descumming. In total, we fabricate nine samples, which receive a descum treatment in PLASSYS. Each sample is treated individually with different descum parameters which can be found in Tab. 4.2.

Samples 'JJ12-064-PM', 'JJ12-067-PM', 'JJ12-068-PM' and 'JJ12-70-PM' have already been evaporated before the measurements of the test sample 'JJ12-062-PM' are done, so they have been kept at atmosphere for multiple days. This is why only 'JJ12-070-PM' is being measured and annealed as a reference sample for a sample, which is exposed to atmosphere for more than a few hours. Two cautiously treated samples for the measurements are samples 'JJ12-069-PM' and 'JJ12-074-PM', after evaporation they are only exposed to atmosphere for roughly 100 minutes for transfers and a pre-annealing resistance measurement. 'JJ12-069-PM' is stored in vacuum in the load lock of the Alu-EVAP before the annealing process, whereas 'JJ12-074-PM' could only be kept in vacuum in a desiccator due to technical issues. All three samples are annealed in SUPERBOWL at  $200^\circ\text{C}$  in a pressure of  $10^{-7}$  mbar. The results of the measurements can be found in Fig. 4.15. On all three samples a decrease in the junction resistance is measured again. Surprisingly, the relative change

Descum Time/ Acceleration Voltage	30 s	60 s	90 s
60 V	JJ12-067-PM	JJ12-066-PM	JJ12-064-PM
85 V	JJ12-074-PM	JJ12-072-PM	JJ12-075-PM
110 V	JJ12-070-PM	JJ12-069-PM	JJ12-068-PM

**Table 4.2:** Used descum parameters for the different samples. Only the samples 'JJ12-069-PM', 'JJ12-070-PM' and 'JJ12-074-PM' are used for evaporation, resistance measurement, annealing and a second resistance measurement after the annealing.

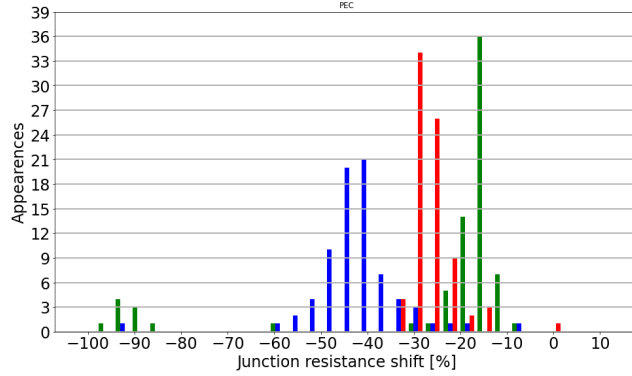


**Figure 4.15:** Relative resistance changes of samples 'JJ12-069-PM' (blue), 'JJ12-070-PM' (green) and 'JJ12-074-PM' (red). More detailed plots of the individual samples can be found in the Appendix in Figs. A.2,A.3 and A.4

of the resistance is the biggest on sample 'JJ12-069-PM' with a decrease of 42.24 %, even though this sample has been assumed to have the best chance to measure a resistance increase, since it has been kept in the best vacuum conditions compared to the other samples. Sample 'JJ12-074-PM' has an lower resistance decrease with a decrease of 25.61%, the lowest resistance decrease is measured on sample 'JJ12-070-PM' with a decrease of 17.15% (The decrease of all junctions of 'JJ12-070-PM' is 26.71%, however, the junctions with an relative resistance decrease of 90-100% are excluded from the calculation of the mean resistance, since they clearly do not belong to the gaussian distribution around 17% seen in Fig. 4.15 and Fig. A.6.).

This unexpected result can be explained by the aging effect of Josephson junctions. The properties of the  $\text{AlO}_x$  barrier are not stable over some time, they can already change over some days significantly due to the absorption or desorption of molecules other than oxygen [19] in the barrier, or by restructuring of the  $\text{AlO}_x$  layers of the barrier [23]. While vacuum conditions slow the aging process down [17], annealing, on the other hand, drives the aging process in a rather short time. This, on the other hand, leads to junctions, with time stable properties since the aging process already is passed due to the annealing.

With this understanding of the aging effect of Josephson junctions, we can conclude, that sample 'JJ12-070-PM', which has not been kept in vacuum conditions, already experienced significant aging until it is measured before the annealing and afterwards again. Therefore, the annealing process itself affects the junction properties less than on the samples 'JJ12-069-PM' and 'JJ12-074-PM'. Among these, sample 'JJ12-069-PM' shows the biggest resistance decrease. This sample is the one, which has been kept in the best vacuum conditions of all three samples. Therefore, the aging effect is reduced in the most possible way, which on the other hand increases the effect of

the annealing in comparison to the other samples.

Another conclusion we draw out of the measurements is, that the absorption of water and the formation of hydroxides into the oxide barrier after the evaporation process cannot be the dominating effect of the reduction of the junction resistance, since avoiding contact of the junctions with the atmosphere showed a more significant reduction rather than a reduction of the resistance decrease. Possibly, during the measurement of the junctions before the annealing and the transfers of the sample at atmosphere, water is already being absorbed by the  $\text{AlO}_x$  layer. This would limit the benefit of keeping the samples in vacuum conditions after the evaporation only to the reduction of the aging of the junctions, as was measured before. Another finding is that structural ordering processes in the  $\text{AlO}_x$  can be the dominant effect compared to the formation of hydroxides inside the barrier. Assuming that a significant amount of the  $\text{AlO}_x$  layer of the insulating barrier are present in an amorphous structure, annealing at a temperature of  $200^\circ\text{C}$  could induce structural ordering processes like annihilation of defects or even crystallization of the aluminum oxides [23] which cause the barrier thickness to decrease. Such structural ordering processes have already been measured at temperatures between  $80^\circ\text{C}$  and  $380^\circ\text{C}$  [23].

For both cases, the conditions of the evaporation process inside the Alu-Evap could be the cause for the water absorption into the oxide barrier or the formation of amorphous  $\text{AlO}_x$  layers. Adapting the evaporation process, for example only evaporating and oxidating in PLASSYS, could result in the desired resistance increase.

# Chapter 5

## Summary and Outlook

### Results

During the course of this thesis, we have adapted the so far established fabrication process of Josephson junctions on  $10\text{ mm} \times 6\text{ mm}$  silicon substrates at WMI for the fabrication on larger  $12\text{ mm} \times 12\text{ mm}$  substrates. This allows for more statistics through junction resistance measurements due to an increase of the amount of junctions on a single substrate from 144 to 420 in total.

The implementation of proximity effect correction (PEC) into the e-beam pattern improved the fabrication process in terms of the limitation of the energy deployment into the resist apart from the areas defined by the junction pattern. The optimal charge dose for the pattern has been determined and results in well defined Josephson junctions.

The reduction of the so far used SQUID loop design to a single junction design allows for a more insightful analysis of the junction properties through the resistance measurements. The added short circuited junctions enable the determination of the intrinsic aluminum resistance and therefore an even more precise calculation of the critical Josephson current  $I_c$  through resistance measurements.

For the implementation of the descum step, reasonable parameters for the descumming process in PLASSYS are found, which create a stable Argon/Oxygen plasma beam. Descumming processes with this plasma beam reduce both the intact resist layer and resist leftovers on the developed areas of the chip by a similar amount. The descumming capacity is confirmed by AFM measurements.

The desired resistance increase as a measure for the removal of resist leftovers could not be observed. However, for all the annealed samples a similar reproducible resistance decrease was measured (17% - 42%), which indicates a general phenomenon occurring in the fabrication process. Since the deposition of water into the tunnel barrier after the evaporation process is not very likely in our system, the actual reason for the resistance reduction still has to be determined. Possible reasons could be the absorption of water already during the evaporation and oxidation processes or

during the resistance measurements of the junctions at atmosphere, or amorphousness of the  $\text{AlO}_x$  layer.

## Outlook

To be able to evaluate the efficiency of the descum step through resistance measurements, one needs to achieve a situation where the expected increase due to the descumming is not covered by other processes decreasing the resistance. For this purpose, two approaches could be investigated: Since the formation of amorphous  $\text{AlO}_x$  layers could be caused by the Alu-EVAP, moving the evaporation and oxidation from the Alu-EVAP into the new PLASSYS system could reduce these effects. A second approach might be an increase of the annealing temperature up to  $400^\circ\text{C}$  and more, since other experiments measure a decrease of the junction resistance of 30% - 40% similar to our data for an annealing temperature of  $200^\circ\text{C}$  but an increase of the junction resistance of 200% - 300% for an annealing temperature of  $400^\circ\text{C}$ . This behaviour is accounted to the dissociation of hydroxides out of the  $\text{AlO}_x$  barrier [21], which therefore leads to an increased barrier thickness and an increased junction resistance.

The evaluation of those two approaches, however, needs further investigation and measurement beyond the framework of this thesis.

# Appendix A

## Plots

## A.1 Resistance Measurements of Sample 'JJ12-062-PM'

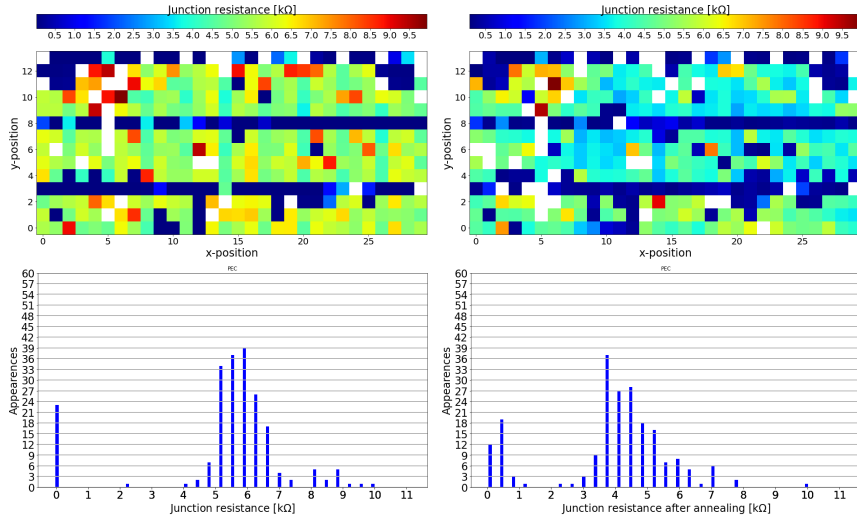


**Figure A.1:** Absolute resistance values measured before and after annealing sample 'JJ12-062-PM'. The two left figures are the measurements before annealing, the two right figures are the measurements after annealing. In the bar chart, only the PEC junctions are listed, the short circuited junctions (three dark rows of the colorplot) and the non PEC junctions are not further investigated.

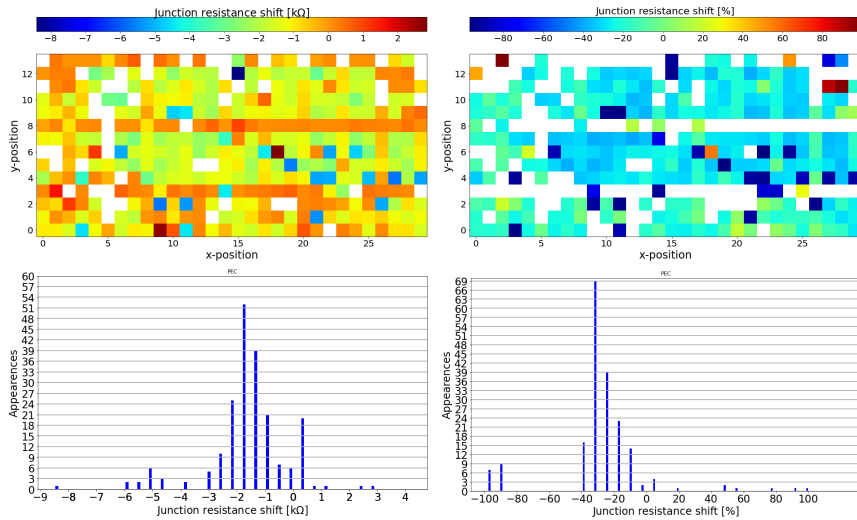


**Figure A.2:** Resistance change due to the annealing of sample 'JJ12-062-PM'. In the bar chart, only the PEC junctions are listed, the short circuited junctions (seen in the three dark rows of the colorplot) and the non PEC junctions are not further investigated.

## A.2 Resistance Measurements of Sample 'JJ12-069-PM'

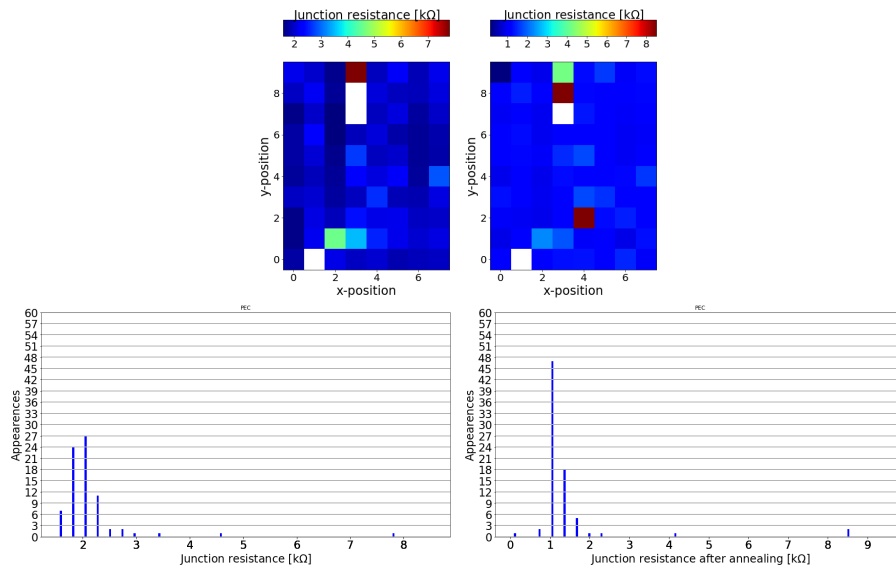


**Figure A.3:** Absolute resistance values measured before and after annealing sample 'JJ12-069-PM'. The two left figures are the measurements before annealing, the two right figures are the measurements after annealing.

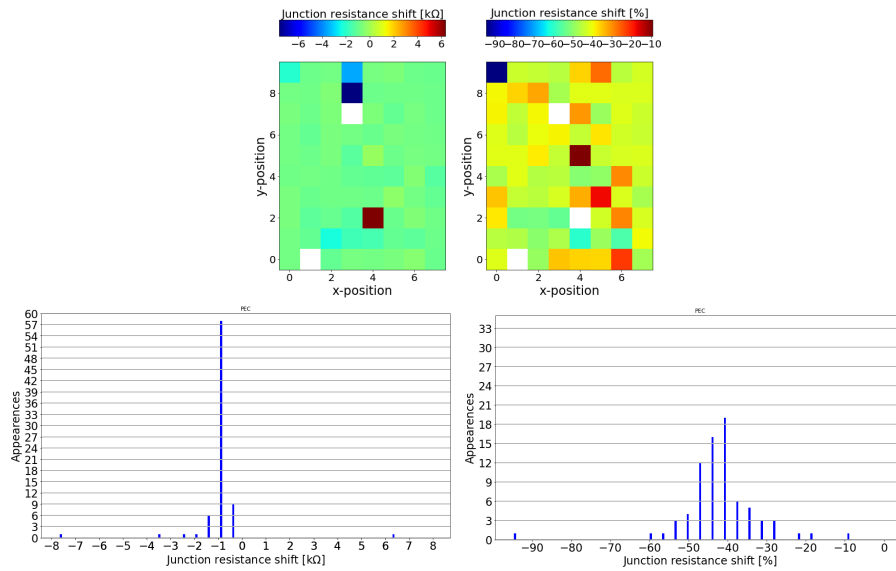


**Figure A.4:** Calculated resistance change due to the annealing of sample 'JJ12-069-PM'.

### A.3 Resistance Measurements of Sample 'JJ12-070-PM'

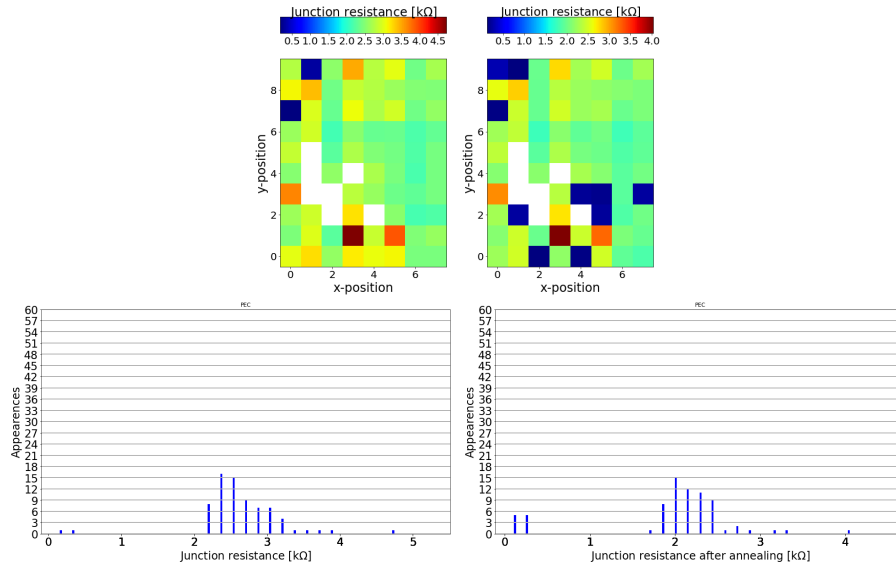


**Figure A.5:** Absolute resistance values measured before and after annealing sample 'JJ12-070-PM'. The two left figures are the measurements before annealing, the two right figures are the measurements after annealing.

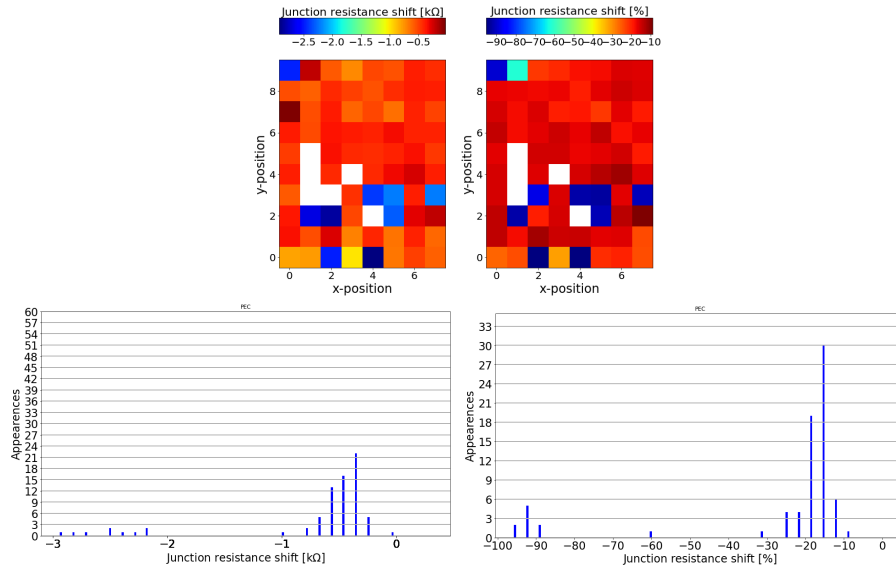


**Figure A.6:** Calculated resistance change due to the annealing of sample 'JJ12-070-PM'.

### A.4 Resistance Measurements of Sample 'JJ12-074-PM'

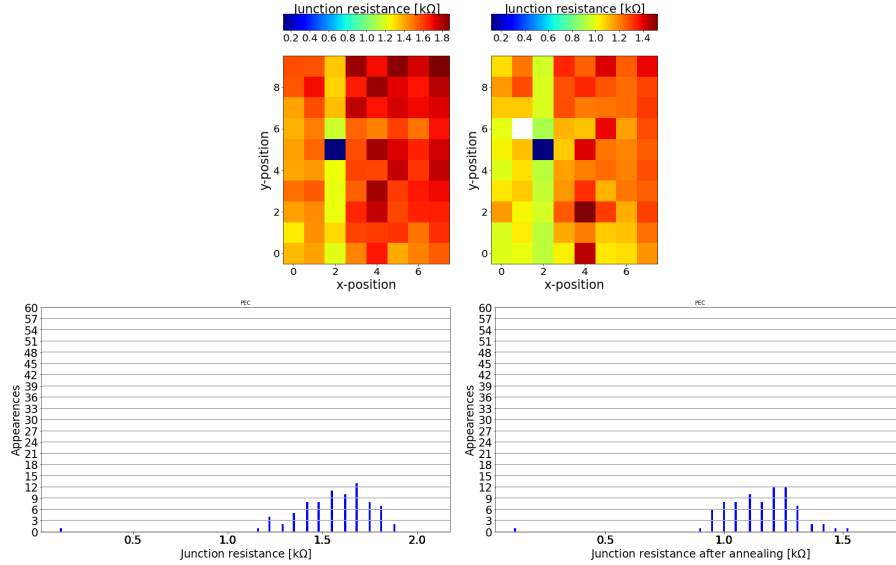


**Figure A.7:** Absolute resistance values measured before and after annealing sample 'JJ12-074-PM'. The two left figures are the measurements before annealing, the two right figures are the measurements after annealing.

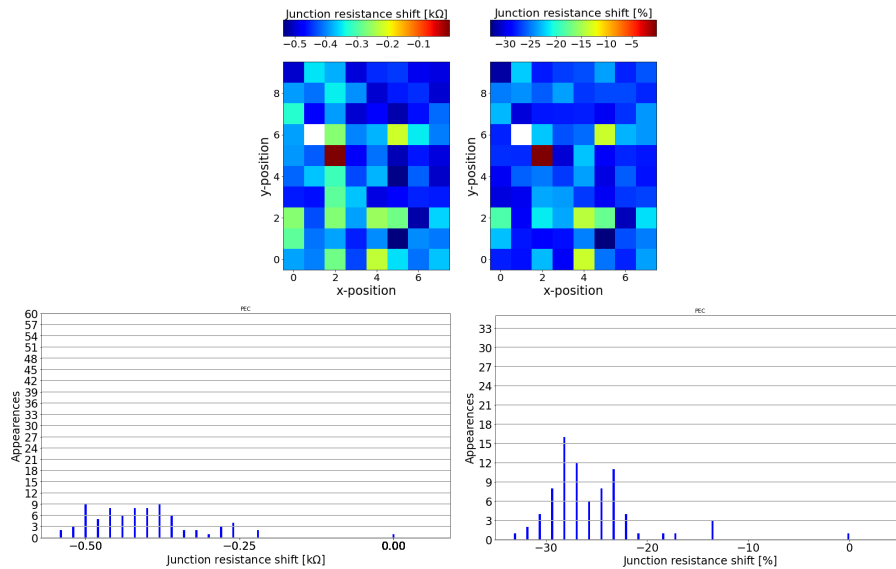


**Figure A.8:** Calculated resistance change due to the annealing of sample 'JJ12-074-PM'.

## Appendix B

### Final Sample Fabrication Parameters

#### B.1 Substrate cleaning

Chemical 1	Acetone
Volume	10 ml
Temperature	70°
Time	10 min
Chemical 2	Acetone
Volume	10 ml
Temperature	70°
Time	10 min
Chemical 3	Isopropanol (IPA)
Volume	10 ml
Temperature	20°C
Supersonic bath strength	9
Supersonic bath time	2 min

**Table B.1:** Cleaning steps for the silicon substrates. The sample is put into the supersonic inside a beaker with isopropanol and afterwards blown dry with a N<sub>2</sub> gun.

## B.2 Reactive Ion Etching (R.I.E.) and post R.I.E. cleaning

General settings	
Pumping pressure (Torr)	$2.0 \cdot 10^{-5}$
RF generator power (W)	100 (98 meas.)
ICP forward power (W)	50 (45 meas.)
APC controller (Torr)	$5.0 \cdot 10^{-2}$
Oxygen ashing	
Oxygen flow (sccm)	50 (49,8 measured)
Argon flow (sccm)	0
Ashing time	180 seconds

**Table B.2:** R.I.E. parameters for the ashing of the silicon substrates.

Chemical 1	Acetone
Volume	10 ml
Temperature	70°
Time	10 min
Chemical 2	Isopropanol (IPA)
Volume	10 ml
Temperature	20°C
Supersonic bath strength	9
Supersonic bath time	2 min

**Table B.3:** Cleaning steps for the silicon substrates after the R.I.E. treatment

### B.3 Spin Coating

Bottom resist	PMMA/MA33%
Volume	350 $\mu$ l
Rotation speed	2000 rpm
Rotation time	120 s
Baking temperature	160°
Baking time	10 min
Top resist	PMMA 950 K A2
Volume	220 $\mu$ l
Rotation speed	2000 rpm
Rotation time	100 s
Baking temperature	200°
Baking time	5 min

**Table B.4:** Spin coating parameters for the top and bottom resist.

### B.4 E-beam lithography

Beam voltage	80 kV
Reference charge dose	12.8 C/m <sup>2</sup>
Ground planes	
Beam current	15 nA - 20 nA
Layers	0-81, 141, 142
Josephson junctions	
Beam current	1 nA - 4 nA
Layers	100-134, 143, 144

**Table B.5:** Parameters for the e-beam lithography. The reference charge dose has to be multiplied with the relative charge dose of each layer to receive the absolute charge dose. The relative charge doses can be found in Fig. B.1

Appendix B Final Sample Fabrication Parameters

---

Relative Charge dose for each layer of JJ12-062-PM.gds

dose 0 0.578500	dose 41 0.870000	dose 100 0.970600
dose 1 0.584300	dose 42 0.878700	dose 101 0.980300
dose 2 0.590200	dose 43 0.887400	dose 102 0.990100
dose 3 0.596100	dose 44 0.896300	dose 103 1.000000
dose 4 0.602000	dose 45 0.905300	dose 104 1.010000
dose 5 0.608000	dose 46 0.914300	dose 105 1.020100
dose 6 0.614100	dose 47 0.923500	dose 106 1.030300
dose 7 0.620300	dose 48 0.932700	dose 107 1.040600
dose 8 0.626500	dose 49 0.942000	dose 108 1.051000
dose 9 0.632700	dose 50 0.951500	dose 109 1.061500
dose 10 0.639100	dose 51 0.961000	dose 110 1.072100
dose 11 0.645400	dose 52 0.970600	dose 111 1.082900
dose 12 0.651900	dose 53 0.980300	dose 112 1.093700
dose 13 0.658400	dose 54 0.990100	dose 113 1.104600
dose 14 0.665000	dose 55 1.000000	dose 114 1.115700
dose 15 0.671700	dose 56 1.010000	dose 115 1.126800
dose 16 0.678400	dose 57 1.020100	dose 116 1.138100
dose 17 0.685200	dose 58 1.030300	dose 117 1.149500
dose 18 0.692000	dose 59 1.040600	dose 118 1.161000
dose 19 0.698900	dose 60 1.051000	dose 119 1.172600
dose 20 0.705900	dose 61 1.061500	dose 120 1.184300
dose 21 0.713000	dose 62 1.072100	dose 121 1.196100
dose 22 0.720100	dose 63 1.082900	dose 122 1.208100
dose 23 0.727300	dose 64 1.093700	dose 123 1.220200
dose 24 0.734600	dose 65 1.104600	dose 124 1.232400
dose 25 0.741900	dose 66 1.115700	dose 125 1.244700
dose 26 0.749300	dose 67 1.126800	dose 126 1.257200
dose 27 0.756800	dose 68 1.138100	dose 127 1.269700
dose 28 0.764400	dose 69 1.149500	dose 128 1.282400
dose 29 0.772000	dose 70 1.161000	dose 129 1.295300
dose 30 0.779800	dose 71 1.172600	dose 130 1.308200
dose 31 0.787600	dose 72 1.184300	dose 131 1.321300
dose 32 0.795400	dose 73 1.196100	dose 132 1.334500
dose 33 0.803400	dose 74 1.208100	dose 133 1.347800
dose 34 0.811400	dose 75 1.220200	dose 134 1.361300
dose 35 0.819500	dose 76 1.232400	
dose 36 0.827700	dose 77 1.244700	dose 140 0.000000
dose 37 0.836000	dose 78 1.257200	dose 141 0.093750
dose 38 0.844400	dose 79 1.269700	dose 142 0.062500
dose 39 0.852800	dose 80 1.282400	dose 143 0.062500
dose 40 0.861300	dose 81 1.295300	dose 144 1.328000

**Figure B.1:** Relative charge doses for each layer of the e-beam pattern file 'JJ12-062-PM.gds'. Each relative charge dose has to be multiplied with a reference charge dose to receive the absolute charge dose.

## B.5 Development

Chemical 1	AR 600-56
Volume	40 ml
Rotation speed	200 rpm
Temperature	20°
Time	30 sec
Chemical 2	Isopropanol (IPA)
Volume	10 ml
Temperature	4° - 4.5 °
Time	10 min

**Table B.6:** Parameters for the development of the sample. The sample is held into the beaker with AR 600-56 facing down with the side with the written structures. The IPA is kept between 4° and 4.5 ° with a peltier cooler.

## B.6 Descumming

<b>Argon flow</b>	5 sccm
<b>Oxygen flow</b>	10 sccm
<b>Descum time</b>	30, 60 or 90 s
Cathode voltage	8.4 V - 8.8 V
Cathode current	6.4 A - 7.3 A
<b>Discharge voltage</b>	40 V (39.8 V meas.)
<b>Beam voltage</b>	200 V (197 V meas.)
<b>Beam current</b>	20 mA (19.6 mA meas.)
<b>Acceleration voltage</b>	60, 85 or 110 V (59, 84 or 109 V meas.)
Acceleration current	6.3, 4.3 or 2.3 mA
Emission	19.6 mA
Neutralizer voltage	10.6 - 10.8 V
Neutralizer current	11.8 - 12.2 mA

**Table B.7:** Descumming parameters used for the ion beam gun (IBG) in PLASSYS. The bold parameters were set as input, the other parameters could not be varied and only the measured parameter values are listed.

## B.7 Evaporation and Oxidation

Evaporation 1	
Pressure	$< 1 \cdot 10^{-7}$ mbar
Evaporation angle	$55^\circ$
Evaporation rate	$10 \text{ \AA/s}$
Aluminum thickness	40 nm
Oxidation 1	
Oxid pressure	$8.1 \cdot 10^{-3}$ mbar
VAT-valve opening	15 %
Oxygen flow	8 sccm
Oxidation time	4.200 s
Evaporation 2	
Pressure	$< 1 \cdot 10^{-7}$ mbar
Evaporation angle	$0^\circ$
Evaporation rate	$10 \text{ \AA/s}$
Aluminum thickness	70 nm
Oxidation 2	
Oxid pressure	$8.1 \cdot 10^{-3}$ mbar
VAT-valve opening	15 %
Oxygen flow	8 sccm
Oxidation time	2.300 s

**Table B.8:** Evaporation and oxidation parameters at the Alu-EVAP.

## B.8 Liftoff

Chemical 1	Acetone
Volume	10 ml
Temperature	70°
Time	60 min
Chemical 2	Acetone
Volume	10 ml
Temperature	70°
Time	60 min
Chemical 3	Isopropanol (IPA)
Volume	10 ml
Temperature	20°C
Supersonic bath strength	1
Supersonic bath time	2 min

**Table B.9:** Parameters for the liftoff of the evaporated samples.

# Bibliography

1. Thew, R., Jennewein, T. & Sasaki, M. Focus on quantum science and technology initiatives around the world. *Quantum Science and Technology* **5**, 010201 (Dec. 2019).
2. Riedel, M., Kovacs, M., Zoller, P., Mlynek, J. & Calarco, T. Europe's Quantum Flagship initiative. *Quantum Science and Technology* **4**, 020501 (Feb. 2019).
3. VDI Technologiezentrum GmbH. *Quantum Flagship* <https://qt.eu/> (2021).
4. Raymer, M. G. & Monroe, C. The US National Quantum Initiative. *Quantum Science and Technology* **4**, 020504 (Feb. 2019).
5. *National Quantum Initiative* <https://www.quantum.gov> (2021).
6. Zhang, Q., Xu, F., Li, L., Liu, N.-L. & Pan, J.-W. Quantum information research in China. *Quantum Science and Technology* **4**, 040503 (Nov. 2019).
7. Bundesministerium für Bildung und Forschung / Federal Ministry of Education and Research (BMBF). Quantum technologies – from basic research to market (Sept. 2018).
8. Krantz, P. *et al.* A quantum engineer's guide to superconducting qubits. *Applied Physics Reviews* **6**, 021318. ISSN: 1931-9401 (June 2019).
9. Orlando, T. P. *et al.* Superconducting persistent-current qubit. *Physical Review B* **60**, 15398–15413. ISSN: 1095-3795 (Dec. 1999).
10. Groß, R. & Marx, A. *Festkörperphysik* ISBN: 978-3-11-055822-7 (De Gruyter, 2018).
11. Ambegaokar, V. & Baratoff, A. Tunneling Between Superconductors. *Phys. Rev. Lett.* **11**, 104–104 (2 July 1963).
12. Scheuer, C. *Fabrication of Superconducting Thin-film Resonators and Josephson Junctions* Master's Thesis, Technical University of Munich (2021).
13. Sterr, F. *Optimization of Josephson Junction Nanofabrication for Superconducting Quantum Circuits* Diploma Thesis, Technical University of Munich (2013).
14. Xie, E. *Optimized fabrication process for nanoscale Josephson junctions used in superconducting quantum circuits* Master's Thesis, Technical University of Munich (2013) ().
15. Wang, L. *Fabrication stability of Josephson junctions for superconducting qubits* Master's Thesis, Technical University of Munich (2015).
16. Goetz, J. *The Interplay of Superconducting Quantum Circuits and Propagating Microwave States* Ph.D. Thesis, Technical University of Munich (2017).

17. Koppinen, P. J., Väistö, L. M. & Maasilta, I. J. Complete stabilization and improvement of the characteristics of tunnel junctions by thermal annealing. *Applied Physics Letters* **90**, 053503. ISSN: 1077-3118 (Jan. 2007).
18. Bilmes, A. *Resolving locations of defects in superconducting transmon qubits* Ph.D. Thesis, Karlsruhe Institute of Technology (2019).
19. Pop, I. M. *et al.* Fabrication of stable and reproducible submicron tunnel junctions. *Journal of Vacuum Science and Technology B, Nanotechnology and Microelectronics: Materials, Processing, Measurement, and Phenomena* **30**, 010607. ISSN: 2166-2754 (Jan. 2012).
20. *BEAMER - Electron- and Laser-Beam Lithography Software, GenISys GmbH, Eschenstr. 66, 82024 Taufkirchen*
21. Scherer, H., Weimann, T., Zorin, A. B. & Niemeyer, J. The effect of thermal annealing on the properties of Al–AlO<sub>x</sub>–Al single electron tunneling transistors. *Journal of Applied Physics* **90**, 2528–2532. ISSN: 1089-7550 (Sept. 2001).
22. Bilmes, A., Neumann, A. K., Volosheniuk, S., Ustinov, A. V. & Lisenfeld, J. *In-situ bandaged Josephson junctions for superconducting quantum processors* 2021. arXiv: 2101.01453 [quant-ph].
23. Pavolotsky, A., Dochev, D. & Belitsky, V. Aging- and annealing-induced variations in Nb/Al–AlO<sub>x</sub>/Nb tunnel junction properties. *Journal of Applied Physics* **109**, 024502 (2011).

# Acknowledgements

First of all I would like to thank **Dr. Frank Deppe**. Not only did he give me the opportunity, to write this thesis in the qubit group at the WMI, but also did he help me stay on course with this thesis and increased the quality of the final version through his corrections a lot.

Second, I want to thank **Yuki Nojiri** for the great job he did as my Advisor. From the first explanations about the fabrication process of Josephson junctions, to various discussions about our results and the next steps of the thesis, he had a very important and positive influence on my work.

Next, I want to thank **Christoph Scheuer**, **Kedar Honasoge** and **Manuel Müller**. Christoph, for providing me the basic python script for the resistance calculations of the Josephson junctions, Kedar for his suggestions how to solve problems occurring during this thesis and Manuel for the towards the end of the thesis concentrated annealing processes at SUPERBOWL.

Also, I want to thank **Johann-Tariq Schlingensiepen**, **Johannes Walcher** and **Tim Edelmann** for keeping my back free in 'StuSta' in quite turbulent times. Especially during the last weeks of this thesis when there was so much happening, they gave me the opportunity to focus fully on the thesis - thank you guys, really.

Special thanks go to my girlfriend, **Sandra Andrusca**, for the mental and physical support during this thesis. Our side-by-side writing sessions always boosted my progress unparalleled and our days off helped me hold the line up to the point where I write this. Thank you. I love you.

Last but not least, I want to thank my parents, **Inge** and **Frank Missale** for giving me the opportunity to study physics in Munich. I would never have been here today, without your support. Thanks for everything.